Evaluation of the Mechanical Properties of Solid Oxide Fuel Cell Materials

Ramakrishna Gwat Koravadi Venkatesha Murthy

A thesis

submitted in partial fulfillment of the requirements for the degree of

Master of Science in Mechanical Engineering

University of Washington

2019

Committee:

Dwayne Arola

Ramulu Mamidala

Junlan Wang

Program Authorized to Offer Degree:

Mechanical Engineering

University of Washington

Abstract

Evaluation of the Mechanical Properties of Solid Oxide Fuel Cell Materials

Ramakrishna Gwat Koravadi Venkatesha Murthy

Chair of Supervisory Committee:
Associate Professor Dwayne Arola,
Department of Materials Science and Engineering

In the pursuit of economic sources of "green energy", Solid Oxide Fuel Cells (SOFCs) are of substantial interest due to their high efficiency, long-term stability, low emissions, and relatively low costs. With a capability of achieving an efficiency of 80%, SOFCs are the most efficient of all the hydrogen fuel cells. These systems operate at high temperatures, often ranging between 500°C and 1000°C. Due to such high operating temperatures, the components of SOFCs are fabricated from ceramic or cermet materials, which exhibit high sensitivity to pores and flaws. Hence, it is important to characterize the reliability and service life of advanced ceramic components at extreme operational environments. Due to their relatively high flaw sensitivity, the mechanical properties of ceramics should be described in a probabilistic manner, to enable a complete description of component reliability.

Magnesia Magnesium Aluminate (MMA) is a candidate ceramic material for high temperature applications including SOFCs. In the present investigation, the strength distribution and Slow Crack Growth (SCG) behavior of a dense MMA manifold material and

porous MMA tube material were evaluated via 4-point flexural testing at temperatures of 20°C, 50°C, and 850°C under wide range of environmental conditions involving exposure to moisture and a mixture of hydrogen and nitrogen gas. A fractographic analysis was performed to identify the origins of failure and as a function of the environment and temperature. It was found that the flexure strength distribution for the dense MMA (proposed as a manifold material) exhibited a Weibull modulus of approximately 11. In addition, at 50°C and 3.5% moisture by volume, the strength displayed significant rate dependence with an SCG exponent of 17, indicating relatively high susceptibility of the material to slow crack growth failures. The flexure strength distribution of the porous MMA (proposed as a tube material) exhibited a Weibull modulus of approximately 10, with large difference between the ambient conditions and high temperature response. At 850°C and within a reformulated fuel environment (50% moisture, 45% nitrogen and 5% hydrogen by volume) the strength displayed significant rate dependence with a SCG exponent of -33, indicating susceptibility of the material to slow crack growth failures. Thermal cycling was found to increase the Weibull modulus of both the dense MMA manifold materials and porous MMA tube materials. Fractography showed that regardless of loading rate or environment, large surface pores resulting from processing were the origins of failure in the weakest samples of both the manifold and tube MMA materials. The results from this investigation should make a significant contribution to the literature concerning the high temperature behavior of structural ceramics.

ACKNOWLEDGEMENTS

I would like to sincerely thank Professor Dwayne Arola for giving me an opportunity to be a part of his research group and guiding me through this research. I learned a lot during these 1.5 years working with him. I am also grateful to Professor Ramulu Mamidala and Professor Junlan Wang for accepting to be members of my thesis committee and for providing guidance to complete this work. I would also like to thank my family and friends for all their support and encouragement.

DEDICATION

To my dear mother, father and sister

for their constant support and encouragement,

and their sacrifices which helped me achieve my dreams.

Table of Contents

LIST OF FIGURES

LIST OF TABLES

CHAPTER 1 : INTRODUCTION

1.1 Overview

1.1.1 Hydrogen Fuel Cells

A Hydrogen Fuel Cell is an electrochemical device that converts the chemical energy from the incoming fuel or hydrogen gas into electrical energy with water as a by-product of the electrochemical reaction. The first fuel cell was developed in 1939 by a British engineer named Francis Thomas Bacon [1]. Hydrogen fuel cell technology is growing in applications as it provides clean energy with minimal or zero emissions, has higher efficiency and lower operational costs, and is easily scalable.

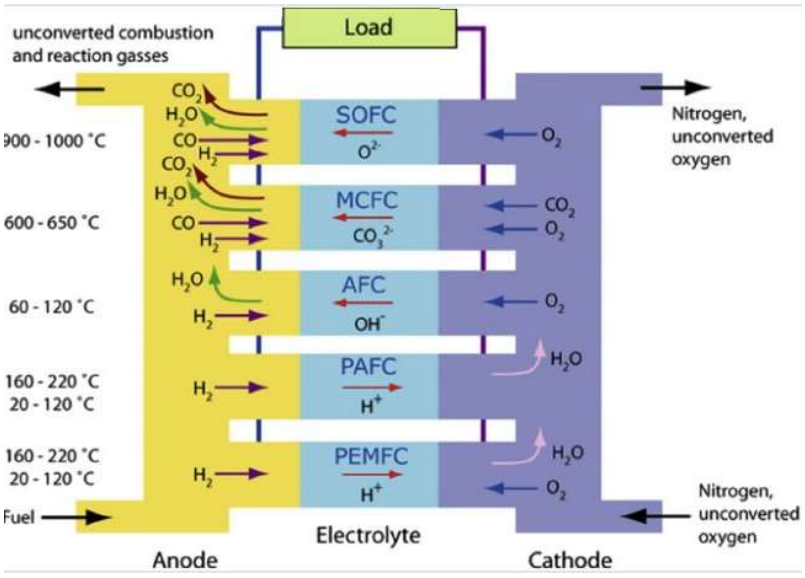

Figure 1.1: Depiction of the working principles of a various types of hydrogen fuel cells [2]

$$2H_2 \rightarrow 4H^+ + 4e^- \tag{1.1}$$

$$O_2 + 4H^+ + 4e^- \rightarrow 2H_2O$$

(1.2)

A fuel cell consists of three major components, viz., anode, electrolyte and cathode. Figure 1.1 depicts the working principle of various types of hydrogen fuel cells. Equations 1.1 and 1.2 are the basic electrochemical reactions of fuel cell that takes place at anode and cathode respectively. Hydrogen gas ionizes at the anode creating H^+ ions while releasing electrons. At the cathode, oxygen from the air reacts with the hydrogen ions to form water. The two electrodes are connected via an electrical circuit through which the electrons flow to produce electrical energy. The hydrogen ions need to travel from the anode to the cathode through the electrolyte to complete this electrochemical reaction.

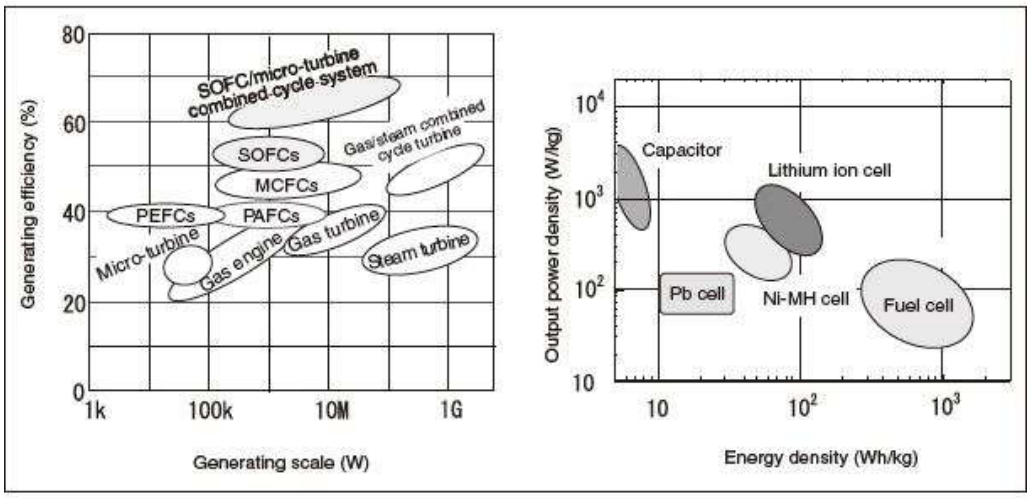

Figure 1.2: Comparison of the efficiencies of various power systems [3]

Figure 1.2 is the comparison chart depicting the generating efficiencies and energy density of various power systems. As evident from Figure 1.2, hydrogen fuel cell systems have higher efficiencies than the commonly used power generation systems like gas turbines and steam turbines. Solid Oxide Fuel Cells in particular can achieve efficiencies upto 70%, with a potential of achieving 80% efficiency.

The hydrogen fuel cells based on the type of electrolyte are classified as follows [4,5]:

- Polymer Electrolyte Fuel Cells (PEFCs): PEFCs utilize a solid hydrated polymeric ion exchange membrane as electrolytes and have carbon electrodes. Hydrogen ions are the primary charge carriers in PEFCs. PEFCs operate in a temperature range of 40°C - 80°C. Platinum is used as a catalyst in PEFCs, and carbon or metal as an interconnect. The primary components of PEFCs are made from carbon-based materials. PEFCs are being pursued mainly as the power source in vehicle and mobile applications. PEFCs have an efficiency of 40% - 50%.
- Alkaline Fuel Cells (AFCs): Solutions of potassium hydroxide prepared in different concentrations in asbestos matrix are used as the electrolytes in AFCs. Hydroxide ions are the primary charge careers in AFCs. AFCs operate in the temperature range of 65°C - 220°C. Platinum is used as a catalyst in AFCs and have metallic interconnects. The primary components of AFCs are made from carbon-based materials. AFCs are being pursued mainly as the power source in space applications. AFCs have an efficiency of around 60%.
- Phosphoric Acid Fuel Cells (PAFCs): Concentrated phosphoric acid is used at the electrolyte in PAFCs. Hydrogen ions are the primary charge carriers in PAFCs. PAFCs operates at a temperature of 220°C. Platinum is used as a catalyst in PAFCs and have graphite interconnects. The primary components of PAFCs are made from graphite-based materials. PAFCs are mainly used in stationary power applications. PAFCs operate at an efficiency of around 40%.
- Molten Carbonate Fuel Cells (MCFCs): MCFCs utilize a combination of alkali carbonates retained in a ceramic matrix of $LiAlO_2$ as the electrolyte. Carbonate ions are the primary charge carriers in MCFCs. MCFCs operates at a temperature of 650°C.

Nickel and nickel oxides are used as catalysts and interconnects in MCFCs. The primary components of MCFCs are made from stainless steel-based materials. MCFCs are mainly used in large stationary power stations and marine applications. MCFCs operate at an efficiency of ~50%.

- Solid Oxide Fuel Cells (SOFCs): SOFCs are all ceramic fuel cells. They use solid ceramic material as an electrolyte. SOFCs utilizes oxide ceramics or perovskites as the electrolytes. Oxygen ions are the primary charge carriers in SOFCs. Ceramics or cermets are used as the electrodes in SOFCs. Nickel, steel or ceramics are used as the interconnects in SOFCs. SOFCs operate in a temperature range of 500°C – 1000°C. SOFCs are mainly being used in stationary power stations and also being pursued for mobile applications. SOFCs have an efficiency of around 60% with potential to achieve and efficiency of 80%.

1.1.2 SOFC Design and Operation

Solid Oxide Fuel Cell (SOFC) is a type of hydrogen fuel cell in which all the components are fabricated from ceramics or cermets. SOFCs are the most efficient of all the hydrogen fuel cells with a capability of achieving an efficiency of 80% and also have a very high life expectancy of over 40,000 hours. SOFCs have really high operating temperatures ranging between 500°C and 1500°C. Operating at such high temperatures is profitable as it promotes rapid electrocatalysis without the use of expensive noble metal catalysts, and produces high quality byproduct heat for co-generation [1]. Most of the SOFC components are made of ceramics or cermets due to such high operational temperatures. Pure hydrogen or hydrocarbons can be used as the fuel for the SOFCs.

Figure 1.3 depicts the operation of a SOFC. A unit of SOFC is mainly composed of two electrodes (anode and cathode) and a solid oxide ceramic electrolyte. The primary function of the anode is to disperse the hydrogen gas equally over its surface and conduct the electrons freed from hydrogen molecules. The primary function of the cathode is to distribute the incoming oxygen on its surface and conduct the electrons from the external circuit to generate oxygen ions. The primary function of the electrolyte is to transport the oxygen ions generated at cathode to anode to complete the electrical circuit. Another major function of the electrolyte is to prevent the two electrodes from coming in electrical contact with each other by blocking the flow of electrons through it. In SOFCs, oxygen ions travel from cathode to anode unlike the other hydrogen fuel cells, in which the hydrogen ions travel from anode to the cathode through the electrolyte.

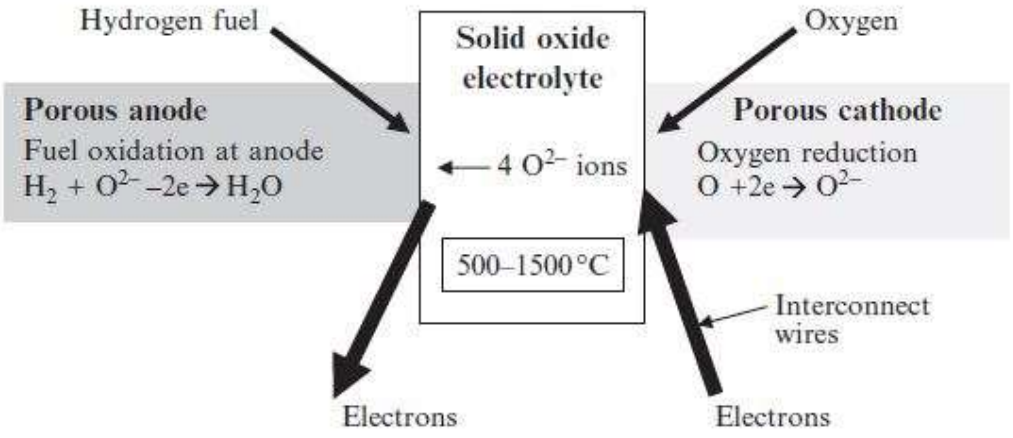

Figure 1.3: Schematic diagram of a SOFC [6]

There are two major designs for SOFCs, viz., tubular and planar. Figure 1.4 depicts the unit cell structure of planar and tubular SOFC. Tubular designs consist of an electrolyte tube sandwiched between the two electrode tubes. It operates with the fuel on the outside and the oxidant on the inside of the tube [1]. Tubular design have good mechanical strength and sealing

convenience [7], but have relatively small interconnection between the serial cells in a stack, which results in large external ohmic losses [8]. It is also difficult to fabricate tubular fuel cells [7] . In the planar design, flat plates of end plates, cathode, electrolyte and anode are bonded and placed over each other to form a stack with the interconnect plate connecting the two-unit cells. During the operation, hydrogen and air flow down channels in the bipolar plates, with one face of each electrode in contact with either the fuel or air [7]. The planar SOFCs can be either electrode supported, or electrolyte supported. A planar SOFC design has short current path between unit cells, relatively low ohmic losses, but has an operating temperature ranging between 800°C - 1000°C, which may lead to gas mixing at the electrodes [8]. Planar SOFCs are relatively easy to fabricate.

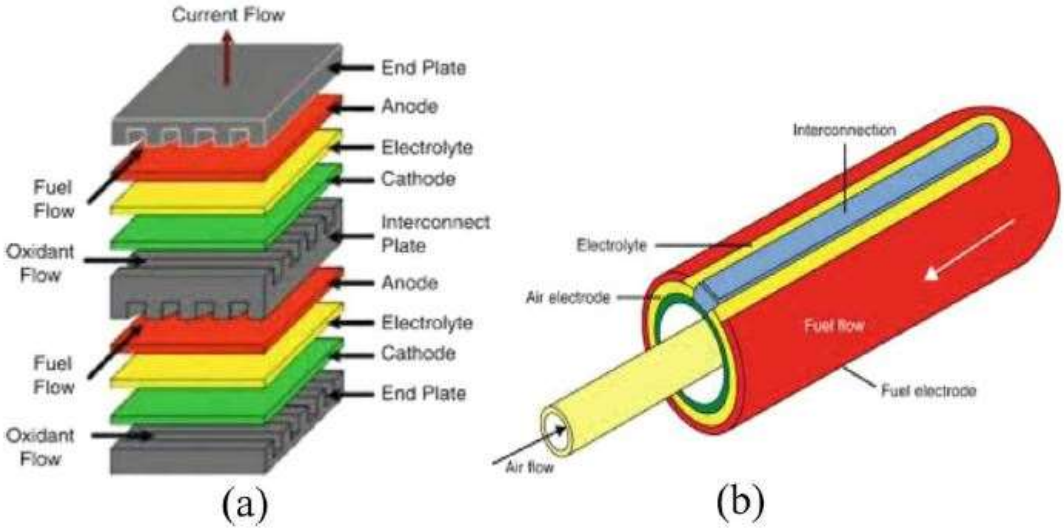

Figure 1.4: SOFC design: (a) Planar ; (b) Tubular [9]

As an unit cell can only generate a small amount of electricity, a stack of cells is formed to generate desired output voltage by connecting cells with one other in series using an interconnector plate [10]. Interconnector plate connects the cathode of one cell with the anode

of another cell. Edges of cell layers, interconnects and individual cells are sealed gas-tight to prevent the gases from mixing and also provide electrical insulation.

Component part	Required properties
Electrolyte	High ionic conductivity, Long-term high temperature performance stability, Density, High long-term reliability (high strength, high durability)
Fuel electrode	Large reaction field (water formation), Numerous paths for electron and ion conduction, Appropriate porosity (smooth migration of hydrogen and formed water), High temperature stability
Air electrode	Large reaction field (oxygen absorption, ionization), Numerous paths for electron and ion conduction, Appropriate porosity (oxygen migration), High temperature stability
Separator	Density, Electron conductivity, High temperature/chemical stability
Cell stack	Sealability (gas shielding between electrodes), Strong bonding between materials and absorption of differences in thermal expansion, Low reactivity between component parts

Figure 1.5: Material property requisites for SOFC components [3]

Figure 1.5 is the list of the material property requirements for various components of a Solid Oxide Fuel Cell. Electrolytes need to have low electronic conductivity, stability under oxidizing and reducing atmospheres, good mechanical and thermal properties at operating temperatures [8]. YSZ is currently the most commonly used electrode material for SOFCs [11], in the temperature range of 850°C - 1000°C. LSGM and LBGM are the other electrode materials with good properties at high operating temperatures. Ceria based electrolytes are used for intermediate temperature applications [8]. Ni-YSZ cermet is commonly used anode material, due to its features like high conductivity, structural stability and compatibility with other materials [11]. LSM, LSM/YSZ composites and GDC coated LSM/YSZ materials are

commonly used as the cathodes in SOFCs [11]. Interconnects act as the physical barrier to prevent unwanted mixing of air and fuel, along with providing electrical connection between the two adjoining unit cells. Therefore, an interconnect needs to have excellent electrical conductivity, chemical stability, good thermal conductivity and thermal expansion compatibility [8]. Interconnects are commonly made form lanthanum chromite oxide doped with other elements [8].

Stresses at any time in SOFCs are dependent on the external loads, thermal fields, coefficient of thermal expansion of the component materials, chemical expansions [12] and also the environment inside the SOFC (i.e., temperature, moisture and gases). SOFC components are subjected to stresses whose magnitude and distribution are functions of cell geometry, temperature distribution and external loads. These stresses are mainly classified into three types[13]. They are:

- Residual stresses: Stresses induced to mismatch in thermoelastic properties of adjoining materials/components and differences in manufacturing processes / heat treatment of the components. Residual stresses are also induced on the components during the staking of cells.
- Thermal stresses: Thermal stresses are the operational stresses induced on the components due to the temperature gradients, and also due to the mismatch in coefficient of thermal expansion between different components. Components may experience thermal shocks in case of sudden or emergency shutdown of the SOFC system.
- External stresses: External stresses are the mechanical stresses induced in the components from applied mechanical loads. These stresses can be induced during stacking different cells together, or during assembly of the SOFC unit.

The strength and mechanical reliability of the SOFC components are dependent on the material properties and other factors like material processing, machining, loads, temperature and environmental conditions [14]. From detailed evaluations of the materials at operating conditions and loads, the component design and manufacturing processes can be optimized. Such evaluations are conducted in the present work to assist in the development of candidate materials for a particular commercial fuel cell assembly.

1.2 Strength Distributions in Ceramics

Fractures in the ceramic materials usually initiate from the flaws and pores distributed throughout the material [15]. These flaws are generally formed in the material during the processing or machining of the material [16]. Flaws are also present in the materials in the form of voids and large foreign particles [17]. The strength of the material varies from sample to sample as it is dependent on the size of the of the major flaw which varies from sample to sample [15]. Due to this randomness in the distribution of flaws throughout the material, ceramics exhibit large scatter in the measured fracture stresses. Therefore, the strength of ceramic materials is measured using probabilistic approach. Gaussian, Weibull and lognormal distributions are the major functions used to define the strength distributions of ceramic materials [18]. Weibull distribution is the most widely used among the three.

Rice et al. [19] classified the defects in ceramics causing failure in materials as follows:

1. Processing defects
    - Pores or porous regions
    - Foreign particles
    - Large grains

2. Machining and handling defects
3. Service or Environmentally induced defects

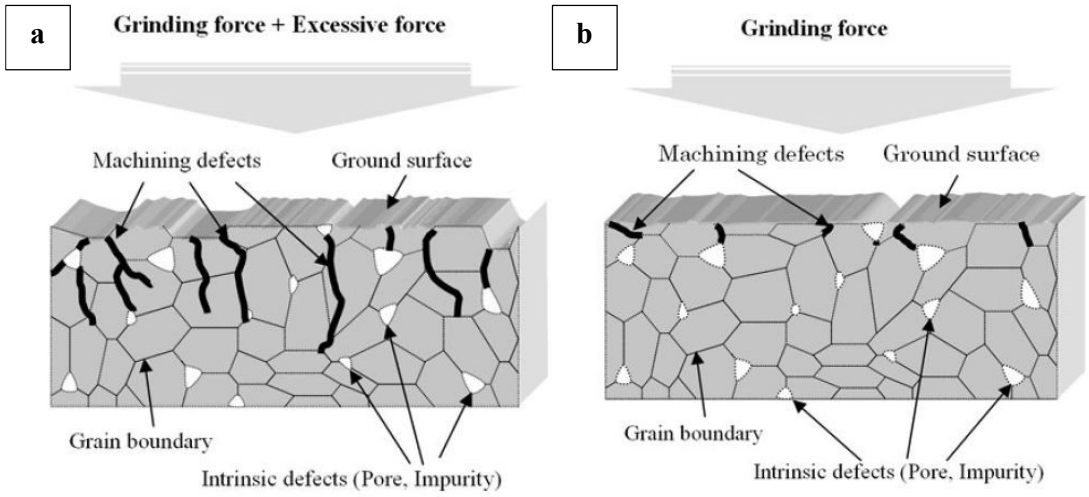

Figure 1.6: Schematic depiction of the damage caused during grinding using : (a) constant speed feeding system; (b) regulated force feeding system [20]

Large flaws in the ceramics are usually introduced during sintering and machining (grinding or polishing) [17]. As grinding and polishing involves the use of abrasive particles, it can lead to two types of cracks, viz., discontinuous series of cracks extending into the material parallel to the groove, and the series of cracks perpendicular to the direction of tool / abrasive motion [19]. Kim et al. [20] evaluated the two grinding methods for ceramics and their effect on the mechanical properties of alumina. They observed that the fracture strength of alumina decreases with the increase in the feeding depth. They also found that the fracture originates from the large machining defects caused due to the use of excessive forces during machining as depicted in Figure 1.6. They also noted that the failures didn't originate from the machining defects when only the grinding force (zero excessive force) was applied on the material during grinding.

The pores can also be the origins of failure under tensile loading in the ceramic

materials [21]. Rice [22] studied the relationship between the porosity and tensile properties of ceramics in general, and developed mathematical models for the same. He reported that the pore shape and size have no influence of the tensile properties when the pores are smaller than the grain size, while the pores with size greater than the grain size can degrade the strength of the material. He also found that the location of pores can play important role in the tensile response. Specially the pores on the grain boundaries can be detrimental due to their propensity to lead to grain boundary cracking which may result in linking of cracks on the intersecting grain boundaries.

The mechanical properties of the ceramics are usually evaluated by performing compression or flexural tests [23]. Tensile tests are rarely conducted on ceramics due to their brittle nature. ASTM C1161 standard defines test method for evaluating the flexural strength for advanced ceramics at ambient conditions [24]. 3-point and 4-point-1/4-point flexural evaluations are covered in this standard. Figure 1.7 depicts the two possible fixtures for 4-point-1/4-point flexural tests. There is no ASTM standard for the evaluation of advanced ceramics at the high temperatures and under environment containing moisture and gas. ASTM C1161 standard is used for such evaluations as well.

The fracture strength of the ceramics is usually analyzed by weakest link hypothesis, which states that the material fails if its weakest volume element fails [25]. Weibull analysis, which is based on the weakest link hypothesis, developed over 70 years ago by Weibull is widely used to characterize the strength distributions of ceramic materials [15].

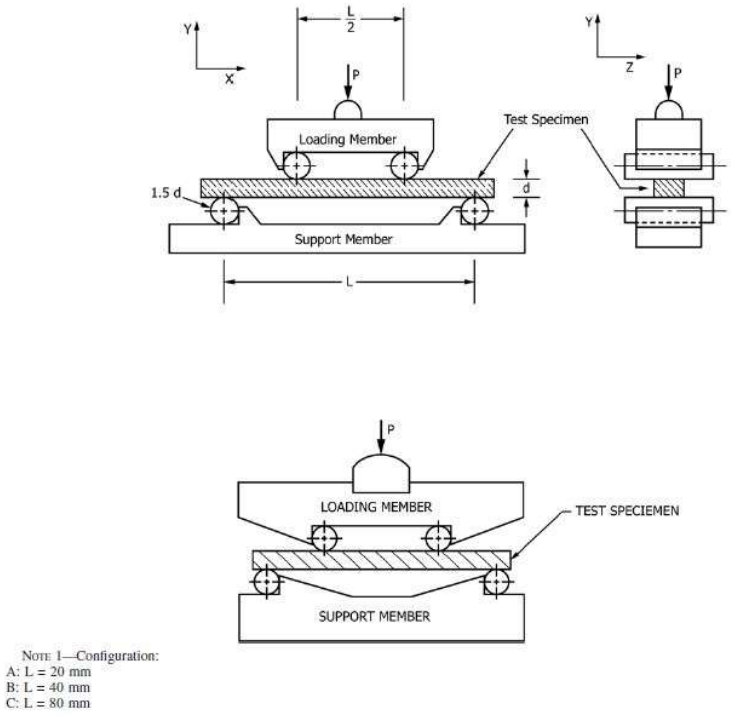

Figure 1.7: Schematics of two suitable fixtures for 4-point-1/4 flexural testing [24]

The probability of failure (P_f) for an applied stress 'σ' according to the Weibull's model is given by Equation 1.3. Equation 1.3 is a 3 parameter Weibull model with the 3 parameters being the Weibull modulus 'm', Characteristic strength or Modulus of Rupture (MoR) 'σ_o'and the threshold strength 'σ_u'. 2-parameter Weibull model is represented by Equation 1.4, in which the threshold strength of the material is assumed to '0'. Figure 1.8 is a Weibull plot of SiN with probability of failure (%) on the vertical axis and the bending strength (MPa) on the horizontal axis. The survival probability in the quality control is measured as 1-P_f.

$$P_f = 1 - e^{-(\frac{\sigma-\sigma_u}{\sigma_o})^m} \tag{1.3}$$

$$P_f = 1 - e^{-\left(\frac{\sigma}{\sigma_o}\right)^m} \tag{1.4}$$

The Weibull modulus is the slope of the best fit line of the Weibull plot as evident in Figure 1.8. The Weibull modulus represents the mechanical reliability of the material at the environmental and loading conditions it was evaluated under. The reliability of the material increases with the increase in the value of 'm'. The material is the most reliable when the value of 'm' is ∞, i.e., when the best fit line of the Weibull plot is vertical, which means that all the samples failed at the same stress. The material is the least reliable when the value of 'm' is 0, i.e., when the best fit line of the Weibull plot is horizontal, which implies that the material can fail at any applied stress making in completely unreliable.

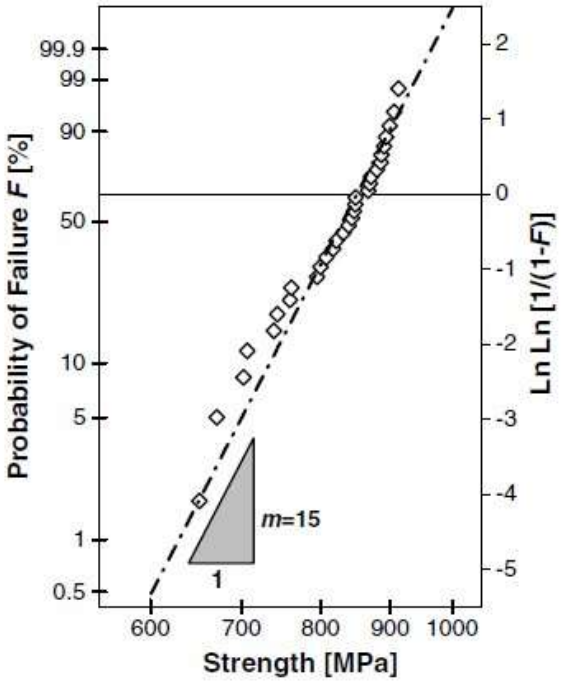

Figure 1.8: Probability of Failure versus Strength in a Weibull Diagram of SiN [15]

The characteristic strength, Modulus of Rupture (MoR), is the stress at which the probability of failure of the material is 63.2%. The threshold strength is the stress below which the material doesn't fail. Two parameter Weibull analysis is widely used for analyzing the strength distribution of ceramics, as it seems to better reflect the observed behavior than the

three parameter Weibull model [15]. Three parameter Weibull analysis, though provides information on the threshold strength of the materials, which will very beneficial in designing the ceramic components.

The Weibull analysis is applicable only when the material is homogeneous throughout the structure, defect population is random, the types of defects are the same in every samples and only one failure mechanism is in operation for all the samples in a batch [26]. In the present work, two parameter Weibull model is used to analyze and compare the strength distributions of MMA SOFC materials at a range of temperatures and environments.

1.3 Slow Crack Growth

In most of the ceramic materials, crack initiation, slow crack growth/subcritical crack growth and rapid/unstable crack growth of fracture are the three stages of fracture [27]. The cracks initiate at the subcritical cracks or defects in the material under stresses lower than the critical stress. Due to the influence of the applied stress, the crack grows at a slow rate until the stress intensity factor (K_I) at the crack tip equals the critical stress intensity factor (K_{IC}) of the material leading to rapid crack growth and hence the failure of the material. Figure 1.9 is a typical logarithmic plot of crack growth rate vs stress intensity, depicting the three regions of a brittle failure. The stress intensity factor is a function of applied stress, crack length and a dimensionless constant which is dependent on the flaw size, location and orientation. Equation 1.4 is the formula used for calculating the stress intensity factor at the crack tip. In the first region, crack originates from the preexisting flaws in the material on the application of load. The crack propagates in this region at a faster rate (v). The crack propagates at slower rate in the second region. The rate of change of crack growth rate is very less in this region. The crack

propagates the fastest in the third region travelling almost at the speed of sound. Rapid crack growth stage is the shortest phase of a brittle fracture. Crack initiation accounts for 20% to 80% of the lifetime of ceramic components [27]. The slow crack growth makes strength of the structural components time dependent. Therefore, it is very important to understand the slow crack growth behavior of materials, predict the failure time based on existing flaws and loading conditions and design the components accordingly [28].

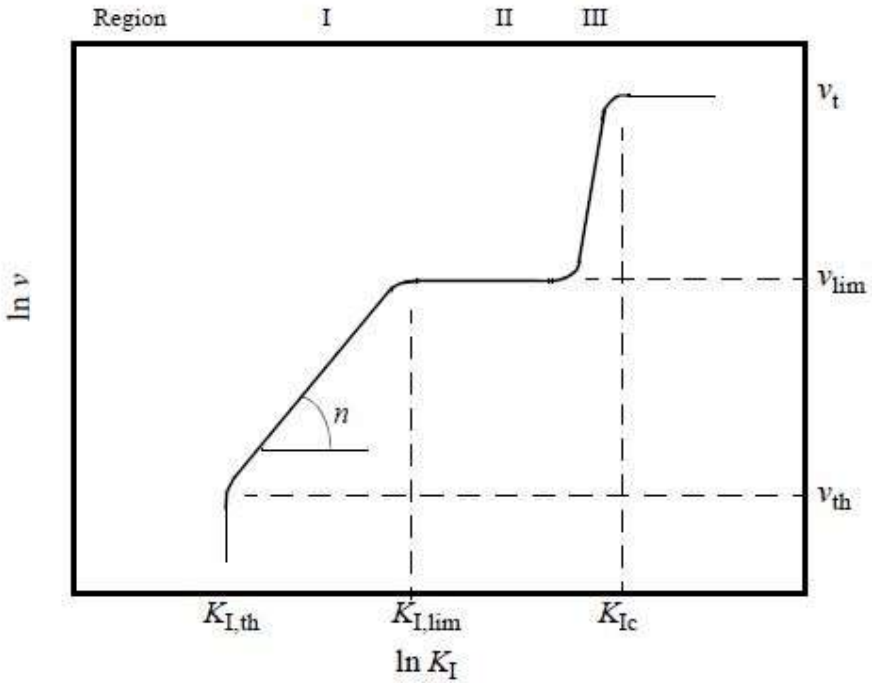

Figure 1.9: Typical double logarithmic plot of crack growth rate vs stress intensity [29]

In ceramics, the slow crack growth can occur due to external loading or also due to environmentally assisted mechanisms like stress corrosion or diffusive crack growth at high temperatures in presence of water vapors and gases. The reactive molecules in the environment can enter the pores or cracks in the ceramics and react with the stretched bonds at the crack tip leading to premature failure. The reactive molecules can break the bonds at the crack tips in two different ways, viz. reaction of reactive molecules with the stretched bonds and by

adsorption [29]. Figure 1.10 depicts the two methods of breaking bonds in ceramics. The reactive molecules such as water, hydrogen, nitrogen, etc. can break the strained bonds at the crack tip and lead to slow crack growth as depicted in Figure 1.10 (a). These molecules can also be adsorbed onto the newly formed surfaces by the extension of crack and hence lower the surface energy, leading to a higher rate of crack growth and hence premature failure as depicted in Figure 1.10 (b).The sensitivity of the material to the moisture and partial pressure of the gaseous molecules determine the extent of slow crack growth in ceramics.

In the oxide ceramics like zirconia and silicon oxide, under stress in the extreme environments, stress corrosion takes place when reactive molecules from the environment like hydrogen atoms from water molecules react with the material and break metal oxide bonds in the material [31,32]. When stresses are applied, bonds at the crack tips are strained, leading to the crack propagation at lower loads than those needed to reach the typical fracture toughness of the material [29].

Van Der Laag [29] had investigated the effect of environment on the fracture properties of alumina and magnesium aluminate. He reported that the exposure to moisture at low and moderate temperatures drastically reduces the fracture toughness of alumina and magnesium aluminate (dense and porous). He also reported that the fracture toughness of dense magnesium aluminate was inversely proportional to the grain size and that the pores have influence on the fracture behavior of porous magnesium aluminate.

Rice et al. [32] investigated the extent of environmentally induced slow crack growth in alumina, magnesium aluminate and magnesia. They reported that the single crystal alumina exhibits slow crack growth, while single crystal magnesia does not exhibit slow crack growth in the presence of water. They also found that the single crystal magnesium aluminate displays

lower slow crack growth than the single crystal alumina in the presence of water. They also reported that polycrystalline magnesium aluminate exhibit transgranular slow crack growth.

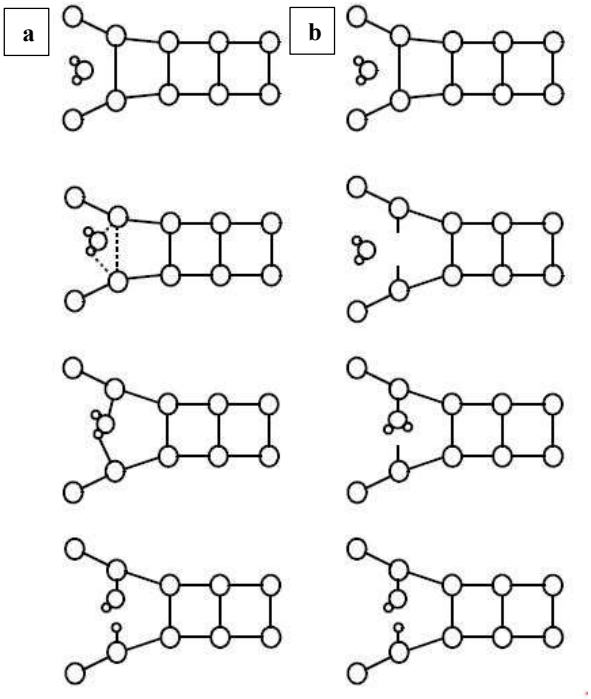

Figure 1.10: Schematic representation of bond breaking processes in oxide ceramics : (a) transition state formation ; (b) adsorption [29]

Hence, MMA with 38 wt.% alumina, which is constituted of magnesia, alumina and magnesium aluminate, is expected to undergo slow crack growth under extreme environmental conditions. It is important to characterize the strength distribution and the slow crack growth properties of the candidate MMA materials as the long-term reliability of SOFCs is dictated by the fracture behavior of the materials.

The slow crack growth parameters of the candidate materials were determined as per ASTM C1368 standard [24]. The slow crack growth is approximated by the empirical power law relation and is related to the rate of crack growth at the crack tip. Equations 1.5 – 1.13 represent the steps in deriving the empirical power law equations [24, 34].

$$v = \frac{da}{dt} = A\left(\frac{K_I}{K_{IC}}\right)^n$$

(1.5)

$$K_I = Y\sigma\sqrt{a}$$

(1.6)

where 'v' is the crack growth rate at the tip of the flaw of size 'a'. 'A' and 'n' are the slow crack growth parameters. 'K_I' is the mode I stress intensity factor at the crack tip and 'K_{IC}' is the mode I fracture toughness of the material. 'σ' is the applied stress at the crack tip and 'Y' is a dimensionless constant which is dependent on flaw size, location and orientation.

From the Equations 1.5 and 1.6 and with manipulations, the relationship between the inert strength 'σ_i' and the fracture strength 'σ_f' is determined.

$$\sigma_f^{n-2} = \sigma_i^{n-2} - \frac{1}{B}\int_0^t \sigma(t)^n \, dt$$

(1.7)

$$B = \frac{2{K_{IC}}^2}{AY^2(n-2)}$$

(1.8)

In the present work, constant stress rate tests were conducted. Therefore $\sigma(t) = \dot{\sigma}t$, where $\dot{\sigma}$ is the stress rate at which the samples are being evaluated. Substituting this in the Equation 1.7 and making some assumptions.

$$\sigma_f^{n-2} = \sigma_i^{n-2} - \frac{1}{B}\int_0^t (\dot{\sigma} t)^n \, dt$$

(1.9)

$$\sigma_f^{n-2} = \sigma_i^{n-2} - \frac{1}{B(n+1)}\dot{\sigma} t^{n+1}$$

(1.10)

Assuming $\left({}^{\sigma_f}/_{\sigma_i}\right)^{n-2} \ll 1$

$$\sigma_f{}^{n+1} = B(n+1)\sigma_i{}^{n-2}\dot{\sigma}$$

(1.11)

$$\sigma_f = D * \dot{\sigma}^{({}^{1}/_{1+n})}$$

(1.12)

$$D = (B(n+1)\sigma_i{}^{n-2})^{({}^{1}/_{1+n})}$$

(1.13)

Equation 1.12 is the empirical power law formula used to find the slow crack growth parameters ('n' and 'D') in ceramics. The time to failure 't_f' of a ceramic material can be estimated using the Equation 1.14.

$$t_f = B\sigma_i{}^{n-2}\sigma^{-n}\left[1 - \left(\frac{\sigma_o}{\sigma_i}\right)^{n-2}\right]$$

(1.14)

1.4 Thermal Cycling of SOFC Materials

The applications of SOFCs are growing day by day and now it is making inroads into automobile industry [34]. e-NV200, the first car powered by a SOFC, being developed by Nissan Motor Corporation is expected to be introduced into commercial markets by 2020 [35].

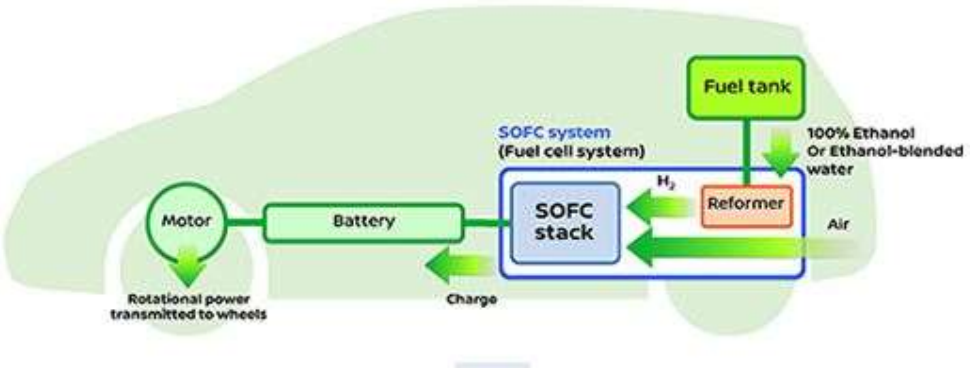

Figure 1.11: Schematic representation of a car run by Solid Oxide Fuel Cells [36]

Figure 1.11 depicts the operation of SOFC run car e-NV200, being developed by Nissan Motor Corporation [37]. In this system, pure hydrogen is produced from the ethanol fuel using a reformer. Energy is generated by SOFC stack utilizing the pure hydrogen generated by reformer and oxygen. The energy generated by SOFC stacks is used to charge a Li-ion battery and the battery will then be used to run the car. e-NV200 is stated to have a driving range of 600+ km for 30 liters of ethanol fuel. As the battery won't be charged continuously, the SOFC stack would not be operating continuously as well, which means that that the SOFC stack will undergo a cycle of heating and cooling every time the battery is charged. Therefore, it is very important to study the effect of thermal cycling on the mechanical properties of SOFC

candidate materials as it would be very useful for choosing the best material, and also for designing and manufacturing the SOFC components.

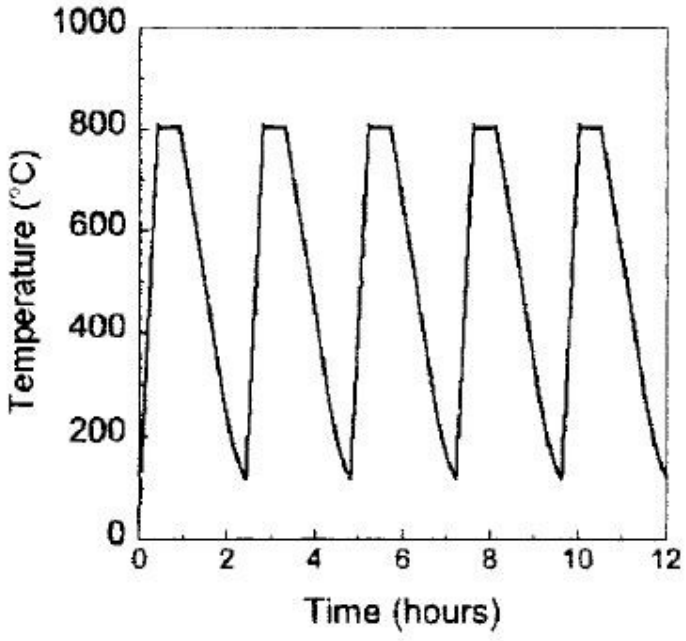

Figure 1.12: Example of thermal cycling schedule [38]

A thermal cycle would involve heating up to desired temperature, holding the material at the desired temperature for certain time and then cooling to lower temperature (usually room temperature). Figure 1.12 is an example of thermal cycling, conducted by Curzio et al. [38] on Ni-YSZ/YSZ bi layer SOFC materials.

Materials undergo a cycle of compressive and tensile thermal stresses during thermal cycling. Equation 1.15 is used to find the deflection 'δ_T'in a material of length 'L'with a coefficient of thermal expansion 'α', when the temperature changes from initial temperature 'T_i' to final temperature 'T_f'. Thermal strain 'ε_T' and thermal stress 'σ_T' are calculated using Equations 1.16 and 1.17 respectively. The unit of 'α' is $K^{-1}$and 'α' is positive for all materials. The temperatures are measured in Kelvins. Figure 1.13 depicts the thermal expansion of a bar

due to increase in temperature and Figure 1.14 depicts the compressive stresses developed in a constrained bar due to increase in the temperature.

$$\delta_T = \alpha(T_i - T_f)L \tag{1.15}$$

$$\varepsilon_T = \alpha(T_i - T_f) \tag{1.16}$$

$$\sigma_T = E\varepsilon_T = E\alpha(T_i - T_f) \tag{1.17}$$

Materials undergo expansion with increasing temperature, and hence if the material is constrained it will experience compressive stress. Equation 1.18 is an example of one such case where the temperature increases from 293 K (20°C) to 1223 K (850°C). Hence, materials will experience compressive thermal forces during the heating phase of a thermal cycle.

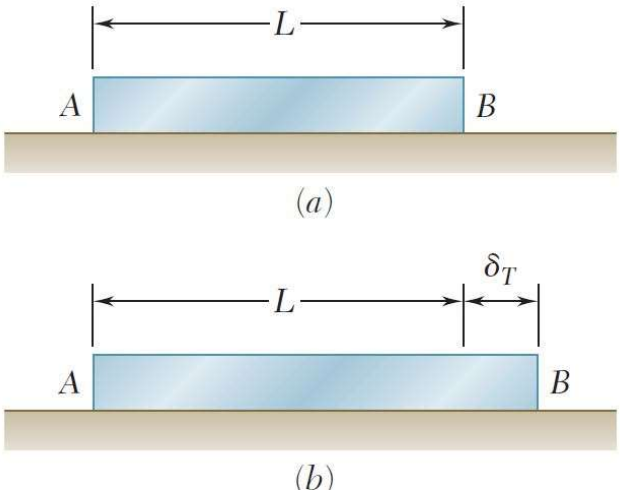

Figure 1.13: Depiction of the expansion of a rod due to temperature increase [39]

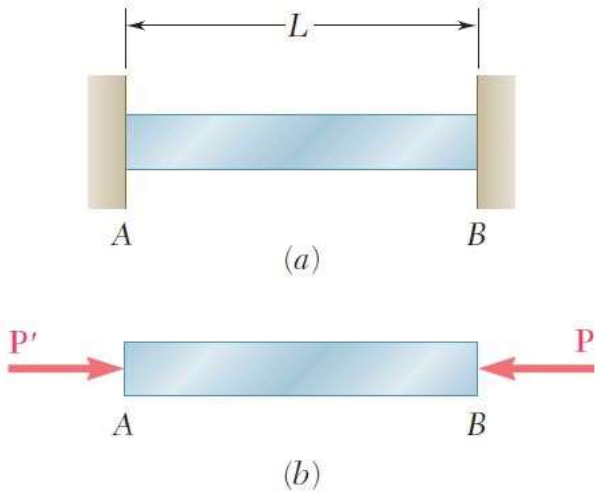

Figure 1.14: Depiction of the stress development in a constrained rod due to temperature increase [39]

$$\sigma_T = E\alpha\left(T_i - T_f\right) = E\alpha(293 - 1223) = -E\alpha(830) \tag{1.18}$$

Materials will undergo contraction when the surrounding temperature is decreased, and hence if the material is constrained it will be under tensile stress. Equation 1.19 is an example of one such case where the temperature decreases to 293 K (20°C) from 1223 K (850°C). Hence, materials will experience tensile thermal forces during the cooling phase of a thermal cycle.

$$\sigma_T = E\alpha\left(T_i - T_f\right) = E\alpha(1223 - 293) = E\alpha(830) \tag{1.19}$$

Rapid cooling can inflict thermal shock on brittle materials like ceramics due to the high tensile stresses acting on the material. There will be a high probability of crack formation and propagation due to the tensile nature of the thermal stress [40]. The resistance of ceramic materials to such thermal shocks are calculated using Equation 1.20. As evident from the

equation, the material with high fracture strength, thermal conductivity and low elasticity and coefficient of thermal expansion can have good thermal shock resistance (TSR). Under rapid thermal shock, the temperature on the surface of the ceramics will be much higher than the interior, resulting in the development of compressive stresses on the surface and tensile stress at the center of cross section of the material, which can lead to crack generation from the center of the material [41].

$$TSR \cong \frac{\sigma_f k}{E\alpha} \tag{1.20}$$

The coefficient of thermal expansion of the two phases of MMA, magnesia and magnesium aluminate are 13.5 x 10^{-6} $K^{-1}$and 7.6 x 10^{-6} K^{-1} [42]. Due to the vast difference in the coefficient of thermal expansion of the constitutive phases, radial microcracks are generated around the inclusions in MMA [43] during the cooling stage of a thermal cycle. Aksel et al. [42] postulated that the microcracks formed due to the thermal shock during the cooling stage inhibit the accumulation of strain energy in MMA. They also reported that the microcracks lead to greater resistance to the degree of damage from thermal shocks and attributed it to the increased difficulty in developing strain energy to propagate the microcracks.

In the present study, the thermal cracking of MMA materials is evaluated at SOFC operating temperatures and environmental conditions, in order to better understand the thermal shock behavior of the material under SOFC operating conditions due to its potential applications in automobile industry and also to evaluate the possibility of improving mechanical reliability and slow crack growth properties by thermal cycling.

1.5 Objectives

It is important to understand the mechanical behavior of dense and porous MMA to maximize its commercial applications as a candidate fuel cell material and beyond. Four-point flexural tests were performed to study the mechanical properties of the new candidate materials at temperatures of 20°C, 50°C, and 850°C under extreme environmental conditions involving exposure to moisture, nitrogen and hydrogen. The objectives of the present study are the following:

- Evaluate the strength distributions, mechanical reliability and slow crack growth behavior of the candidate dense MMA manifold and porous MMA tube materials at ambient and extreme operational conditions and correlate these properties with the microstructure and porosity of the materials.
- Study the effect of thermal cycling on the strength distributions, mechanical reliability and the slow crack growth behavior of the candidate dense MMA manifold and porous MMA tube materials and correlate these properties with the microstructure and porosity of the materials.
- Study the effect of creep (or stress healing) on the strength distributions and mechanical reliability of the porous MMA tube material.

CHAPTER 2 : MATERIALS AND METHODS

2.1 Materials

Magnesia Magnesium Aluminate (MMA) with 38 wt.% alumina was used for the present study. Dense MMA manifolds and porous MMA tubes used for the present study were supplied by LG Fuel Cell Systems (LGFCS), based in Canton, Ohio. The materials were received from LGFCS in the form of the SOFC components. Figure 2.1 depicts one such fuel cell with porous MMA tube with dense MMA end caps.

Figure 2.1: A single unit of a SOFC developed by LGFCS [14]

MMA also known as magnesia rich spinel is an advanced ceramic material widely used in high temperature refractory applications [30]. MMA has high melting point, high chemical inertness, high thermal resistance and high corrosion resistance against slags, good strength at ambient and elevated temperatures, and moderate expansion values at high temperatures [45–47]. MMA is widely used in refractory applications like cement rotary kilns and steel making vessels [31, 48]. Batrakov et al. [48] reported that the thermo-mechanical properties of MMA are the best when the alumina content ranges between 28 wt.% and 70 wt.%. MMA used for the present study had 38 wt.% of alumina, in the range that is reported to produce best thermo-mechanical properties.

Figure 2.2 depicts the equilibrium phase diagram of $MgO/MgAl_2O_4/Al_2O_3$ system. This system involves three widely used ceramics, viz., Magnesia (MgO), Alumina (Al_2O_3) and Magnesium Aluminate ($MgAl_2O_4$). In the phase diagram depicted in the Figure 2.2, magnesia and alumina are the two variable phases. The portion marked as 'S' in the diagram is the region of spinel phase, which is widely used in various high temperature applications [30]. The region marked with 'M+S' on the phase diagram represented in the Figure 2.2 is the region of our interest, as it consists of magnesia and magnesium aluminate phases. The material used for the present study has 38% of alumina by weight, which implies that material undergoes phase transformation at 2050°C. So, MMA with 38 wt.% alumina can be utilized for applications with temperatures up to 2050°C. As the SOFCs generally operate at temperatures around 500°C-1500°C, it is feasible to use MMA materials in SOFCs.

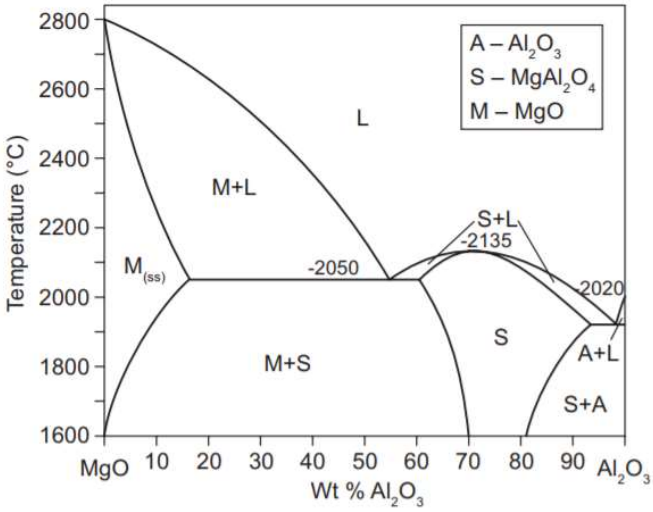

Figure 2.2: Phase diagram of $MgO/MgAl_2O_4/Al_2O_3$ system [49]

2.2 Sample Preparation

Samples for the evaluation of the mechanical properties were prepared from the SOFC components using Chevalier Smart-H818II surface grinder shown in the Figure 2.3. Chevalier Smart-H818II is a 3-axis conversational CNC, with options for semi-automatic and manual operations. Chevalier Smart-H818II has a table size of 203.2 mm x 457.2 mm, and a maximum spindle speed of 3450 rpm. Diamond cutting wheels/blades with a diameter and thickness of 150 mm and 0.46 mm respectively, consisting of 320 mesh abrasives were used to prepare the test samples. The diamond cutting wheels/blades were supplied by Hickerson Industries, Woodland Hills, California. A liquid solution consisting of water and Rustlick WS-5050 cutting oil was used as the coolant to reduce heat while preparing samples.

A hub was mounted on the spindle. A pair of aluminium slingers was mounted on the hub with the diamond cutting wheel between them. This was followed by locking hub-slinger assembly onto the spindle using a threaded nut. Slingers with a diameter 110 mm were used to achieve minimal deflection of the diamond wheel.

The material to be sectioned was mounted on a steel plate using 3M Heavy-duty double-sided foam tape. The mounting plate was then placed on the magnetic table of the Chevalier surface grinder. After the proper aligning of the MMA mounted steel plate, it was locked onto the table surface by activating the magnetic chuck. The feed rates and the limits of the lateral movement of the table were set based on the material nature and dimensions.

The steps described above were common for both the dense MMA manifolds and porous MMA tubes. These steps were followed by slicing of the components into smaller parts out of which the actual flexural test specimens were prepared using specific inbuilt functions.

These steps are described in the sub-sections to follow. The samples were prepared as per ASTM C1161 standards.

Figure 2.3: Chevalier Smart-H818II surface grinder used for the sample preparation

2.2.1 Dense MMA Manifolds

The dense MMA exhaust manifolds were received in the form of 457 mm long components as shown in Figure 2.4. Two different sets of materials, including M3 and M4 manifolds (LGFCS designation) were received. The manifolds had 4 longitudinal channels of width (15.5 mm x 7 mm). The manifolds had a regular pattern of machined slots on one of the faces (referred to as the bottom face) of the component. Material chipping was noticed on the inner surface of the bottom face in the area near the machined slots.

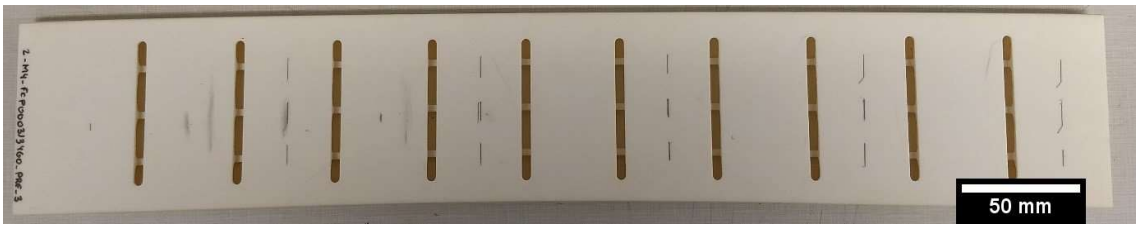

Figure 2.4: Bottom face of a dense MMA manifold component supplied by LGFCS

The 457 mm long components were first sliced into five equal sections of length 80 mm and 2 sections of length 28.5 mm each as depicted in the Figure 2.5. The 80 mm long sections were further sliced to prepare 4 mm wide test samples as depicted in the Figure 2.5. A total of 40 flexural test specimens were prepared from each dense MMA manifold component.

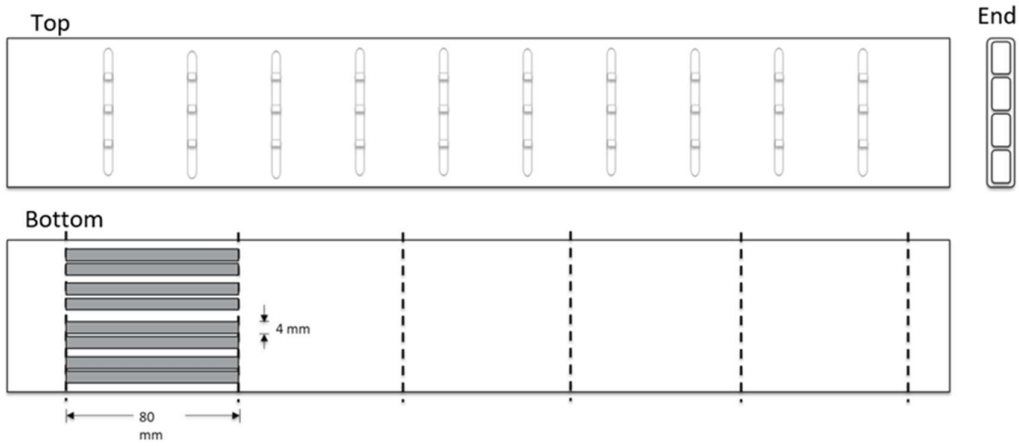

Figure 2.5: Diagram of a dense MMA manifold supplied by LGFCS [14]

The bottom face of the as-received dense MMA manifold components was attached to the steel plate using a 3M double-sided adhesive tape and placed on the table of Chevalier surface grinder as described in the previous section. An inbuilt function, 'MOBN' was used to slice the as-received component into five 80 mm long sections and two 28.5 mm long sections. The material was sliced through the depth of the manifold in multiple passes at a feed rate of 25.4 mm/min. The depth of cut was set at 0.508 mm for each pass. This was repeated until the as-received component was completely sliced into seven different sections.

The five 80 mm sections were further sliced to prepare flexural test specimens. The bottom face of the section (the face containing sectioned slots) was attached to the steel plate using 3M double-sided adhesive tape and placed on the table of Chevalier surface grinder as described before. An inbuilt function, 'GA02' was used to slice the dense MMA manifold sections. The top surface of the upper face of the dense MMA manifold sections was used as the tensile surface for the flexural tests to be consistent and eliminate any effect of slicing in the results. The material was sliced through the depth of top face in one pass at a feed rate of 1.27 mm/min. The depth of cut, which is the equal to the thickness of the top face, varied from component to component, ranging between 1.5 mm to 3 mm. Each channel had a width of approximately 11 mm. So, two samples were sliced from every channel of a section. This process was repeated until the all possible samples were sliced from all the five 80 mm sections in the component. A total of 40 flexural test samples were prepared from one dense MMA manifold component supplied by LGFCS.

The faces sliced by the diamond cutting wheels were polished using 800 grit polishing paper in water to remove defects if any introduced during the preparation of the samples. Few samples did not possess consistent cross-section. So, those samples were polished accordingly using 800 grit polishing paper, along the two sliced faces and the bottom face to achieve the rectangular cross-section. It must be noted that the top surface which would serve as the tensile surface during flexural tests was not polished.

Post the completion of polishing, both the dense MMA manifold samples were dried at 120°C for two hours, to remove moisture from the samples. This was followed by firing of the samples at 1060°C for two hours using a Thermolyne bench-top furnace, as recommended by LGFCS. Any adhesive remaining on the samples was completely removed during the firing process. This process also aided in removal of the manufacturing defects on the samples.

2.2.2 Porous MMA Tubes

The porous MMA tubes were received as 245 mm long components in the form shown in Figure 2.6. Two different sets of materials, porous MMA tubes and Ceracomb tubes (LGFCS designations) were received from LGFCS. The MMA tubes had a total of 15 channels. The two channels at the two ends had non regular cross sections as depicted in the Figure 2.7. The other 13 channels had rectangular cross-sections. The cross section of these 13 channels was 2.83 mm x 1.43 mm.

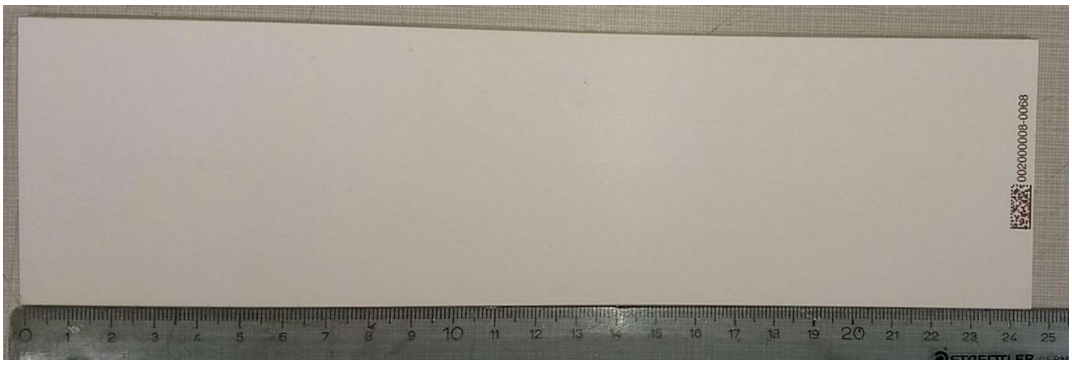

Figure 2.6: A porous MMA tube component supplied by LGFCS

The 245 mm long components were first cut into 4 sections of length 61.25 mm as depicted in Figure 2.7. Four 12.65 mm wide flexural test samples depicted in Figure 2.7 were then sliced from each of the four 61.25 mm long sections. A total of 16 flexural test samples were prepared from each porous MMA tube component.

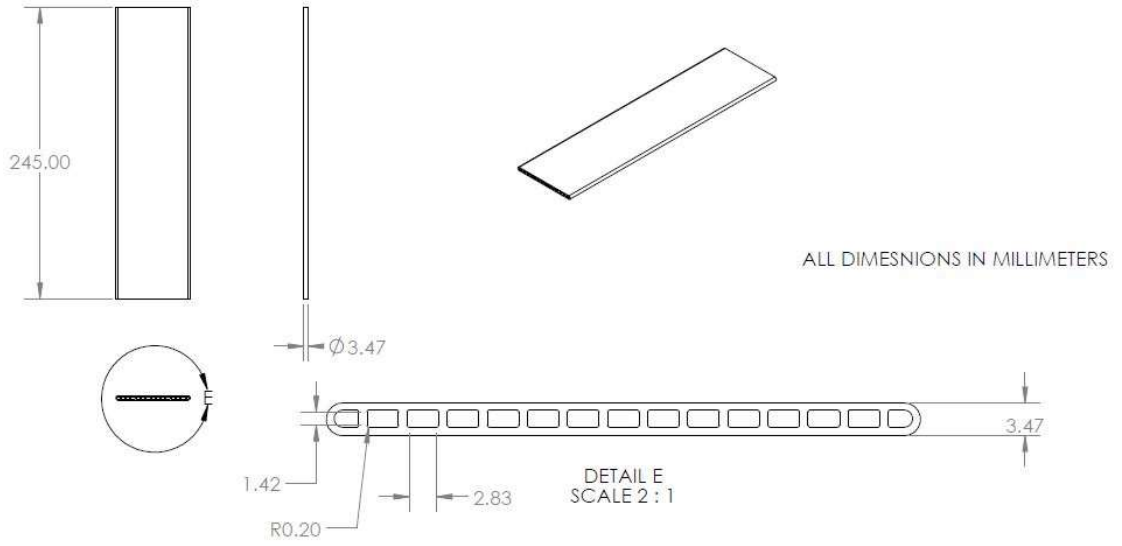

Figure 2.7: Drawing of porous MMA tubes supplied by LGFCS

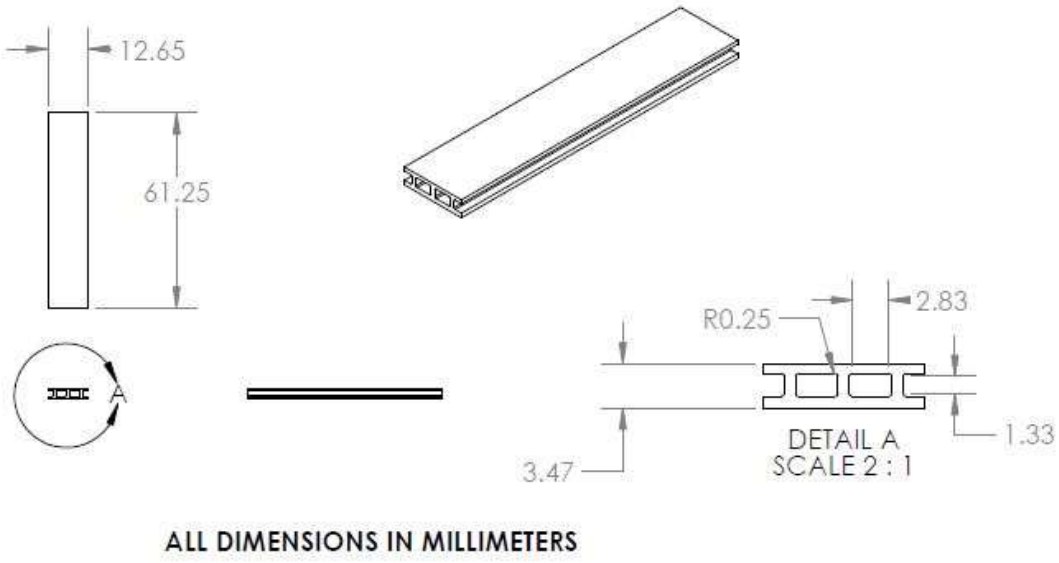

Figure 2.8: Drawing of a porous MMA tube test specimen

One of the faces from the porous MMA tube component was chosen as a bottom face. The bottom face of the as-received porous MMA tube component was attached to the steel plate using a 3M double-sided adhesive tape and placed on the table of Chevalier surface grinder as described in the previous section. An inbuilt function, 'MOBN' was used to slice

the as-received component into four 61.25 mm long sections. As the material was porous and hence less dense compared to the dense MMA manifold material, higher feed rates were used to prepare to slice the porous MMA tubes. The material was sliced through the depth of the component in multiple passes at a feed rate of 35.56 mm/min. The depth of cut was set at 0.508 mm for each pass. This was repeated until the as-received component was completely sliced into four different sections.

The four 61.25 mm sections were further sliced to prepare flexural test specimens. The bottom face of the section was attached to the steel plate using 3M double-sided adhesive tape and placed on the table of Chevalier surface grinder as described before. An inbuilt function, 'MOBN' was used to slice the porous MMA tube sections. The top surface of the upper face of the porous MMA tube sections was used as the tensile surface for the flexural tests to be consistent and eliminate any effect of slicing in the results. The material was sliced through the depth of the component in multiple passes at a feed rate of 35.56 mm/min. The depth of cut was set at 0.508 mm for each pass. This was repeated until the four 13.25 mm wide flexural test samples were cut from the 61.25 mm porous MMA tube section. A total of 16 flexural test samples were prepared from one porous MMA tube component supplied by LGFCS.

The faces sliced by the diamond cutting wheels were polished using 800 grit polishing paper in water to remove defects if any were introduced during the preparation of the samples. It must be noted that the top surface, which would serve as the tensile surface during flexural tests, was not polished. Post the completion of polishing, both the porous MMA tube samples were dried at 120°C for two hours, to remove moisture from the samples. This was followed by firing of the samples at 1060°C for two hours using a Thermolyne bench-top furnace, as recommended by LGFCS. Any adhesive remaining on the samples was completely removed

during the firing process. This process also aided in removal of the manufacturing defects on the samples.

2.3 Environment Controlled 4-point Flexural Testing

Four-point-1/4-point flexural tests were conducted on the dense MMA manifolds and porous MMA tubes specimens using an Instron E-1000 UTM, fitted with Thermolyne type 47900 bench top furnace shown in Figure 2.9. The specimens were loaded within the furnace under desired environmental conditions. Moisture analyzer and gas mixture bottle used for achieving required environmental conditions are shown in Figure 2.10.

Figure 2.9: Intron E-1000 UTM loaded with Thermolyne 47900 bench top furnace used for flexural tests.

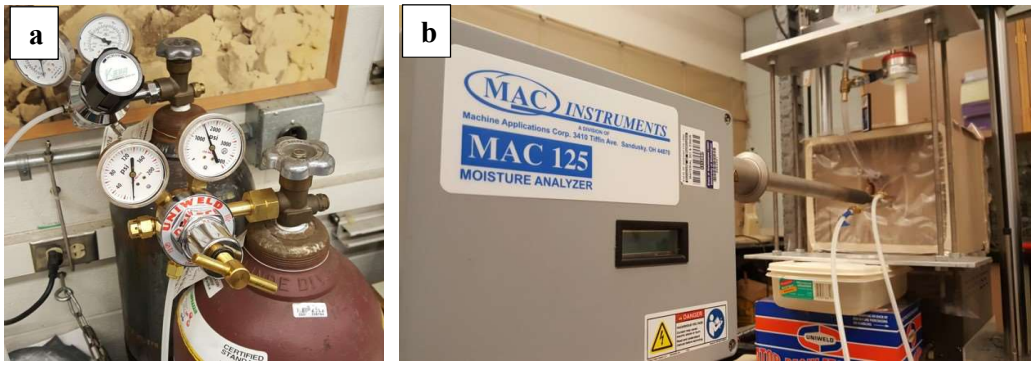

Figure 2.10: Picture of : (a) H_2 and N_2 mixture gas bottle; (b) MAC 125 moisture analyzer used for evaluations of MMA

A four point-1/4-point bend fixture, with an outer span of 40 mm and an inner span of 20 mm, made from high purity alumina was used to conduct the flexural tests. The fixture was based on the ASTM C1161 standard. Figure 2.11 depicts the four point-1/4-point flexural testing setup used for testing of MMA materials. Fixture assembly consisted of a lower fixture, upper fixture, a loading ball, four rollers and a loading rod.

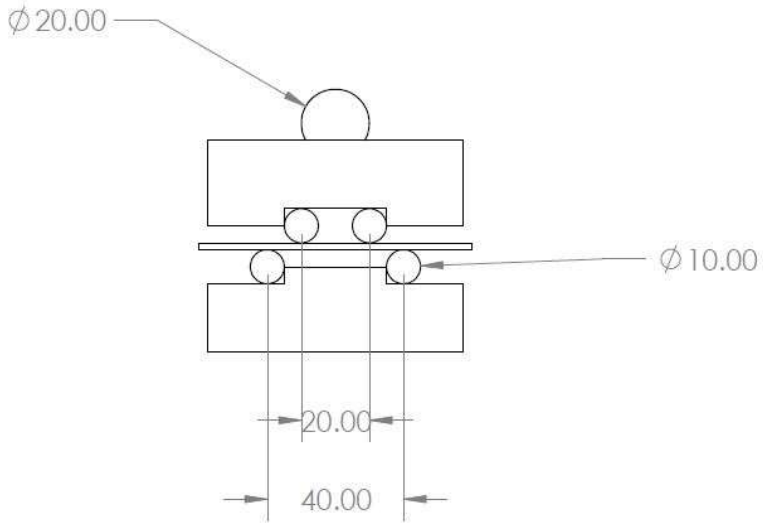

Figure 2.11: Drawing of flexural testing setup (dimensions in mm)

Thermolyne 47900 benchtop furnace with a maximum temperature of 1200°C was used to control the temperature. The furnace was covered by a plastic film (used for vacuum bagging of composites) to contain moisture and gas inside the furnace and hence achieve and maintain the required environmental conditions inside the furnace. Apex Instruments made MAC 125 continuous moisture analyzer was used to monitor the moisture content inside the furnace. MAC 125 moisture analyzer can measure between 0% to 60% moisture by volume, with an accuracy of ±1% moisture by volume and with a response time of 60 seconds. To achieve the required gaseous environment inside the furnace, a premixed gaseous mixture containing 95% nitrogen and 5% hydrogen was supplied to the furnace. A compressed gas cylinder of type UN1956 supplied by Praxair was used for supplying the gas.

The method of setting up the fixture is described below:

- Two rollers were connected to each to each other using a pair of rubber bands. Two pairs of such roller sets were prepared.
- The test specimen was placed between the rollers and placed on the lower fixture.
- The sample and rollers were centered using rulers.
- Upper fixture was then placed on the top rollers. The fixture and the samples were centered again to ensure that fixture is symmetric.
- The fixture assembly was placed inside the furnace. Loading ball was placed in the slot on the upper fixture.
- The fixture assembly was aligned with the loading rod using metal tongs.
- A small compressive preload of ~5N was applied on the fixture assembly.
- All the rubber bands were removed using metal tweezers.
- The preload on the fixture assembly was removed.

After setting up the fixture assembly inside the furnace, the specimens were evaluated at ambient or extreme environmental conditions. The details of the tests are described in the following subsections.

In a 4-point-¼-point flexural test, for a failure load 'P' in Newtons (N) and a support span 'L' in millimeters (mm), the maximum bending moment is given by:

$$M = \frac{F * L}{8} \tag{2.1}$$

Based on Euler's beam theory, the distance between the neutral axis and the bending axis 'c' in millimeters (mm) was assumed to remain constant throughout deformation till failure. The moment of inertia about the axis of bending in mm^4, of the dense MMA manifold samples was calculated using the moment of inertia formula for rectangular cross-sections. The moment of inertia of the porous MMA tube samples were found using parallel axis theorem. The fracture strength 'σ_f' in Mega Pascals (MPa) of the evaluated specimens was found out using the following equation:

$$\sigma_f = \frac{M * c}{I_x} \tag{2.2}$$

2.3.1 Dense MMA Manifolds

Dense MMA manifolds were evaluated under ambient and at 50°C and 3.5% moisture by volume (MBV). Two Honeywell humidifiers were used to achieve the required relative humidity levels. The testing at non-ambient conditions were conducted to mimic the actual working conditions of the material in a SOFC. Such evaluations would produce meaningful

results which can be directly used to make modifications in design and manufacturing of the SOFC components using this material. An Instron load cell with a capacity of 250 N, with loading accuracy of 0.01% was used to conduct flexural tests of dense MMA manifold specimens.

For the evaluations at the ambient environmental condition, the samples were loaded until failure immediately after the fixture assembly was arranged inside the furnace. For the evaluations at 50°C and 3.5% MBV, the furnace was switched on after the fixture assembly was setup in the furnace. After the temperature of the furnace stabilized at 50°C, two humidifiers were switched on to achieve 3.5% relative humidity in the furnace. The fixture assembly along with the sample was soaked at the required environmental condition for 30 minutes. The samples were loaded till failure post this period. Thirty M3 dense MMA manifold specimens each were evaluated at loading rates of 0.09 mm/s and 0.00009 mm/s, under an environment of 50°C with a relative humidity of 3.5%.

2.3.2 Porous MMA Tubes

Porous MMA tubes were evaluated under ambient conditions and at 850°C under an extreme environment. Extreme environment for porous MMA tubes were defined as 850°C in an environment containing 50% moisture, 47.5% nitrogen and 2.5% hydrogen by volume. A dripper arrangement was used to introduce water droplets into the furnace to achieve the required moisture levels in the furnace. An Instron load cell with a capacity of 2 KN, with loading accuracy of 0.01% was used to conduct flexural tests of porous MMA tube specimens.

For the evaluations at the ambient environmental condition, the samples were loaded till failure as soon as the fixture assembly was setup inside the furnace. For the evaluations at

850°C under extreme environmental conditions, the furnace was switched on after the fixture assembly was setup in the furnace. After the temperature of the furnace reached 800°C, water droplets were introduced at a rate of 1 drop every 10 seconds using the dripper arrangement. Once the reading in the moisture analyser started to increase over 5%, the rate of releasing droplets was increased to moisture levels of 50±5 %. Once the required temperature and moisture contents was achieved, the gaseous mixture was introduced into the furnace. The fixture assembly along with the sample was soaked at the required environmental condition for 30 minutes. The samples were loaded till failure post this period.

Six samples of Ceracomb tube specimens were evaluated at a loading rate of 0.009 mm/s under ambient conditions. 30 samples each were evaluated at loading rates of 0.09 mm/s and 0.00009 mm/s, at 850°C under extreme environmental condition.

2.4 Strength Distribution and Slow Crack Growth Analysis

2.4.1 Strength Distribution Analysis

Due to the sensitivity of ceramics to the pores and flaws present in the material, they show considerable variation in strength [31]. Therefore, it is better to evaluate the strength of ceramics using statistical methods instead of a deterministic method. The Weibull weak-link model is a widely used statistical method for analyzing strength distributions in ceramics [50].

The Weibull distribution is a continuous distribution in the form:

$$f(t) = \frac{\beta}{\eta} * (\frac{t-\gamma}{\eta})^{\beta-1} * e^{-(\frac{t-\gamma}{\eta})^{\beta}} \quad (2.3)$$

where 't' is the variable, 'β' is the shape parameter, 'η' is the scale parameter and, 'γ' is the location parameter. The same function when applied to strength distribution becomes:

$$P = 1 - e^{-(\frac{\sigma-\sigma_u}{\sigma_o})^m} \tag{2.4}$$

where 'P' is the probability of failure. 'σ' is the fracture strength of the sample. In addition, 'm' is the shape parameter, also called the Weibull Modulus, which represents the consistency in stress at failure of the material. In general, a higher value of 'm' suggests higher consistency in the defects contributing to failure and also higher reliability of the material, and vice versa. The parameter 'σ_o' is the scale parameter, also called as the 'characteristic strength' or Modulus of Rupture (MoR). This parameter represents the stress at which the probability of failure is 63.2%. Lastly, 'σ_u' is the location parameter, also called as the 'threshold stress'- stress below which there is no failure.

Equations 2.3 and 2.4 are known as the 3 parameter Weibull distributions [51]. In a 2 parameter Weibull distribution, the location parameter 'σ_u' is assumed to be zero. The 2 parameter Weibull analysis was adopted study the strength distributions in the present research.

The median rank method suggested by Kapoor and Lamberson [52] was used to estimate the cumulative probability of failure for a given stress. The measured fracture strengths of the material were ranked in an ascending order, and the median rank was approximated by using the following equation:

$$P_j = \frac{j - 0.3}{n + 0.4} \tag{2.5}$$

where 'P_i' is the median rank, 'j' is the stress rank, and 'n' is the total number of samples in the distribution.

$$ln\left(ln\left(\frac{1}{1-P_j}\right)\right) = m * \ln(\sigma) - m * ln(\sigma_o) \tag{2.6}$$

The cumulative probability of failure at each stress level was found using Equation 2.5. Data was plotted with the logarithm of fracture strength in MPa on the x-axis and the logarithm from of probability of failure on the y-axis. The data was best with a linear approximation as indicated in the Equation 2.6. The slope of the best fit line is the Weibull modulus 'm' of the material, and the characteristic strength, Modulus of Rupture (MoR) in MPa was calculated using the Equation 2.7.

$$MoR = e^{c/m} \tag{2.7}$$

2.4.2 Slow Crack Growth Analysis

The constant stress-rate slow crack growth analysis was performed on the basis of ASTM C1368 standard [53]. Equation 2.8 shows the relationship between the failure stress of the material and the stress rate. In this equation 'D' and 'n' are the SCG properties of a material where 'D' is the SCG coefficient and 'n' is the SCG exponent.

$$\sigma_f = D * \dot{\sigma}^{(1/1+n)} \tag{2.8}$$

$$ln(\sigma_f) = \ln(D) + \left(\frac{1}{1+n}\right) * ln(\dot{\sigma})$$

(2.9)

$$\dot{P} = \frac{Load\ at\ failure - Initial\ load}{Time\ at\ failure - Initial\ time}$$

(2.10)

$$\dot{\sigma} = \frac{3\dot{P}L}{4bd^2}$$

(2.11)

The loading rate and stress rate were calculated using the Equations 2.10 and 2.11 respectively. The SCG response was plotted with the logarithm of failure stress in MPa on the x-axis and the logarithm of stress rate in MPa/s on the y-axis. The data was best fit using linear approximation to find the SCG properties, 'D' in MPa and 'n'.

2.5 Thermal Cycling of Dense MMA Manifolds

Chipping was observed on the inner surface of the bottom face of the as-received dense MMA manifold components. Figure 2.12 depicts chipped regions of one such component. The sectioned manifold components (post the slicing of the test sample from the components) were used as support structures to place the test specimens inside the Thermolyne furnace for 2 hours of firing at 1060°C. It was noticed that the chipping area increased in the components after every cycle and eventually the manifold component cracked after undergoing multiple heat cycles as shown in Figure 2.13.

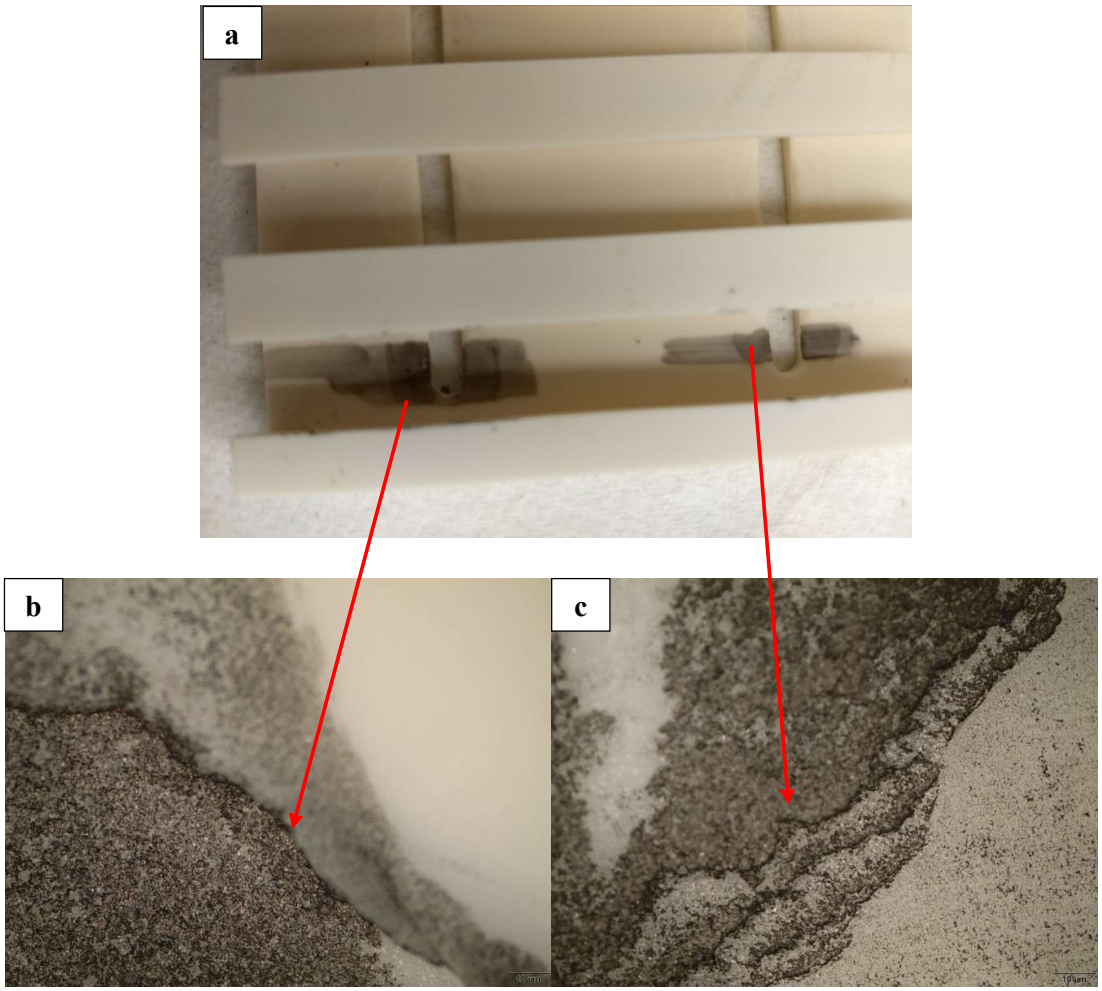

Figure 2.12: Manufacturing induced chipping in dense MMA manifold component ; (a) Picture of manifold component indicating the chipping region; (b) and (c) Magnified optical micrographs of the chipping region

This failure of the dense MMA manifold component was the motivation to perform thermal cycling of dense MMA manifold materials and study its effect on the strength reliability and slow crack growth properties of the material. It was also done to find the root cause for this failure of the MMA manifold components.

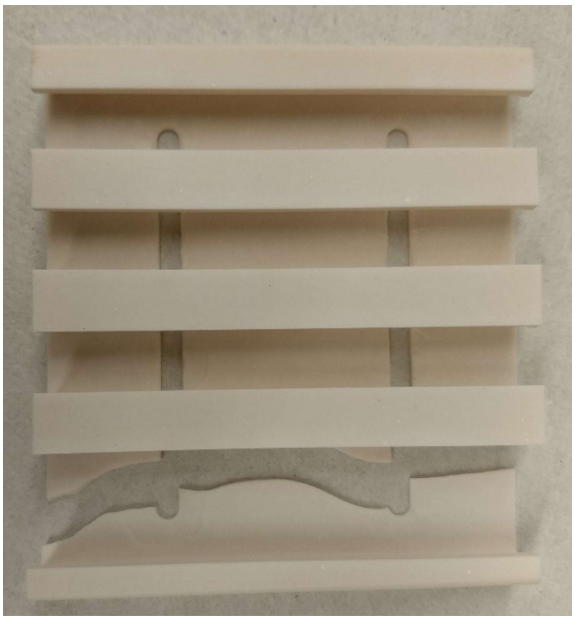

Figure 2.13: Failed dense MMA manifold component, with the chipped region being the origin of failure

The M3 and M4 dense MMA manifold materials were thermally cycled and the effect of thermal cycling on the strength distribution and the SCG properties was studied. A single thermal cycle for dense MMA manifold materials was defined as follows: Heating from the ambient temperature (20°C) till 1060°C at an average rate of 6.93°C / minute. This was followed by soaking at 1060°C for 2 hours and further cooling to the ambient temperature at an average rate of 4.95°C / minute. Heating rate used for the thermal cycling was the default heating rate of the Thermolyne furnace used. Cooling rate of 4.95°C / minute was achieved by opening the furnace door 45 minutes after the furnace was turned off at the completion of soaking period.

Four-point-1/4-point flexural tests of thermally cycled MMA manifold specimens were conducted as described in the section 2.3.1. The details of the tests conducted is given in Table 2.1.

Table 2.1: Details of the flexural tests conducted on the thermally cycled MMA manifold materials

LGFCS designated material name	Number of thermal cycles	Loading rate (mm/s)	Testing conditions	Number of specimens evaluated
M4	1	0.009	Ambient	12
M4	5	0.009	Ambient	6
M4	10	0.009	Ambient	6
M3	5	0.009	Ambient	6
M3	5	0.09	50°C + 3.5% MBV	15
M3	5	0.00009	50°C + 3.5% MBV	15

2.6 Thermal Cycling of Porous MMA Tubes

There is a rapid development of ground transport running on hydrogen. In such vehicles, the SOFC charges a Li-ion battery which in turn runs the vehicle. As the SOFC will be operational only for the time during which the batteries are being charged, it undergoes thermal cycling. In the present study, the porous MMA tubes were cycled in an attempt to mimic the actual operational condition these tubes in SOFCs may undergo.

The porous MMA tubes were made to undergo various thermal cycles. All the thermal cycles had the similar heating phase. The samples were heated from the ambient temperature (20°C) till 850°C at an average rate of 6.92°C / minute. This was followed by soaking at 850°C

and cooling to the ambient temperature. Five samples were evaluated in every batch. The details of the thermal cycles are presented in the

Table 2.2.

Table 2.2: Details of thermal cycling of porous MMA tubes

Test name	**Soaking time (hr)**	**Cooling rate (°C / minute)**	**Number of cycles**
A	2	5.33	5
B	2	5.33	10
C	2	2.31	5
D	2	8.89	5
E	6	2.31	5

Default heating rate of the Thermolyne furnace was used for thermal cycling. An average cooling rate of 2.31°C / minute was achieved by cooling the specimens inside the furnace without any forced convection. An average cooling rate of 5.33°C / minute was achieved by opening the furnace door 45 minutes after the furnace was turned off at the completion of soaking period. An average cooling rate of 8.89°C / minute was achieved by opening the furnace door 45 minutes after the furnace was turned off at the completion of soaking period and forcing the ambient air into the furnace using a Honeywell table fan.

2.7 Evaluation of the Effect of Creep on the Strength Distribution of Porous MMA Tubes

LGFCS noticed that the strength of the porous MMA tube increased when a dead weight was placed on the porous MMA tubes under the operational conditions. This observations by LGFCS was the motivation to study the effect of long exposure of the porous MMA tubes to extreme environmental conditions under stress on the strength distribution of the material. Five samples each of the porous MMA tubes underwent creep at stresses equal to 1% of the MoR, and 50% of the MoR of porous MMA tube material at 850°C in air. The samples were held at the required stress for a period of 24 hours under an environment of 850°C and 50% moisture by volume. Post this, the samples were unloaded and held at that condition for 10 minutes. This was followed by loading till failure at a loading rate of 0.009 mm/s. Five samples were evaluated for both the conditions.

CHAPTER 3 : RESULTS

3.1 Dense MMA Manifold

The strength distributions of the M4 MMA manifold were evaluated at loading rates of 0.09 mm/s and 0.00009 mm/s at 50°C and at 3.5% moisture by volume. The slow crack growth behavior of the M4 MMA manifold material was also characterized at the stated environmental conditions. These results were then compared with the properties of M3 Manifold material evaluated by Stark [14].

3.1.1 Strength Distribution Analysis of M4 Manifold Material

Figure 3.1 showcases the Weibull strength distribution plots of M4 MMA manifold material evaluated at 50°C and at 3.5% moisture by volume. The values of the Weibull modulus, Modulus of Rupture (MoR) and stress range of both M3 and M4 Manifold materials are listed in Table 3.1.

There was minimal reduction of 6% in the Weibull modulus of M4 MMA manifold material with an increase in loading rate from 0.00009 mm/s to 0.09 mm/s. The MoR on the other hand increased from 110 MPa to 165 MPa with the increase in loading rate, implying that the material resisted fracture better at the higher loading rate.

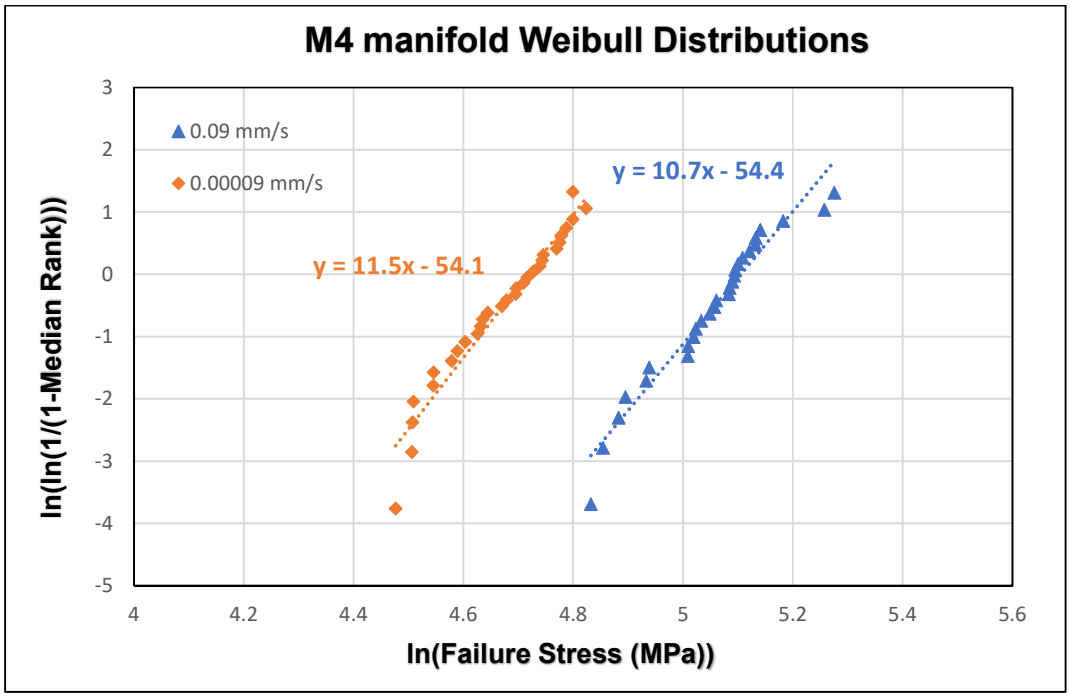

Figure 3.1: Weibull plots of M4 MMA manifold material at various loading rates at 50°C and 3.5% moisture by volume

Table 3.1: Comparison of the Weibull properties of M3 and M4 manifold materials evaluated at 50^0C and at 3.5% moisture by volume

Material	**Loading Rate (mm/s)**	**m**	**MoR (MPa)**	**Average Stress (MPa)**	**Min Stress (MPa)**	**Max Stress (MPa)**
M4	0.09	10.7	164.9	157.4	125.5	195.5
	0.00009	11.5	110.4	107.1	87.9	124.3
M3 [14]	0.09	20.3	161.4	156.6	137.2	170.0
	0.00009	14.4	149.4	144.2	116.9	163.0

As evident from the Table 3.1, M4 MMA manifold material had variations in MoR with changes in the loading rate similar to that in M3 manifold material. But the Weibull modulus increased by 6 MPa (41% increase) when the loading rate was increased from 0.00009 mm/s to 0.09 mm/s unlike M3 MMA manifold material, implying that the failures at fastest loading rate was more consistent compared to the slowest loading rate.

The M3 MMA manifold material had greater Weibull modulus at both the loading rates than the M4 MMA manifold whereas the M4 MMA manifold material had greater fracture strength than the M3 MMA manifold material at both the loading rates.

3.1.2 Slow Crack Growth Analysis of M4 Manifold Material

Figure 3.2 depicts the slow crack growth response of M4 MMA manifold material at 50°C and 3.5% moisture by volume. The material had an SCG coefficient of 126 MPa and an SCG exponent of 17. The low value of the SCG exponent implies that the material is very susceptible to slow crack growth at 50°C and 3.5% moisture by volume. The positive value of the SCG exponent implies that the material flexural strength increases with the increase in loading rate.

Table 3.2: SCG Properties of M3 and M4 Manifold materials

Material	SCG Coefficient 'D'(MPa)	SCG Exponent 'n'
M4	125.9	16.9
M3 [14]	149.1	81.6

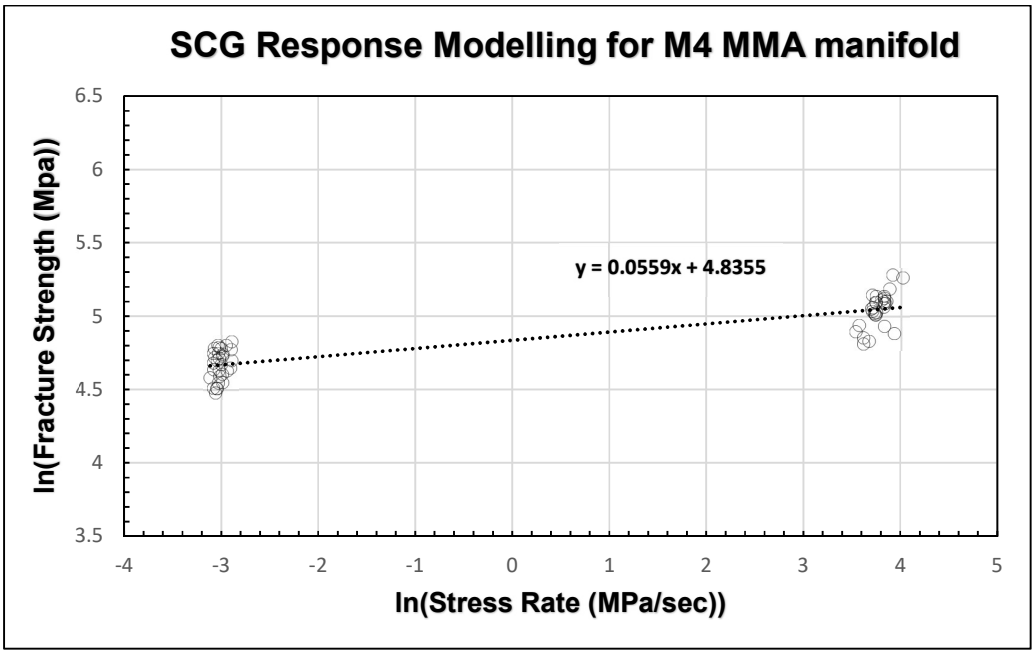

Figure 3.2: SCG plot of M4 MMA manifold material at 50°C and 3.5% moisture by volume.

As evident from the Figure 3.2, M3 manifold material had an SCG exponent of 82, which is greater than that of M4 manifold material, implying M4 MMA manifold material is more prone to slow crack growth than the M3 manifold material. M4 manifold material had a lower SCG coefficient than the M3 manifold material implying that fracture toughness of M3 manifold material was greater than that of M4 manifold material.

3.1.3 Fractography

Figure 3.3 is the Scanning Electron Micrograph of the fracture surface of M3 and M4 MMA manifold materials [14]. The M3 manifold material had grain sizes ranging between 9 and 13 microns whereas the M4 manifold material had grain sizes ranging between 10 and 21 microns. As evident from the Figure 3.3, the M3 MMA manifold material failed by

intergranular fracture, while the M4 MMA manifold material exhibited a mixed mode fracture, displaying features of both transgranular and intergranular fracture.

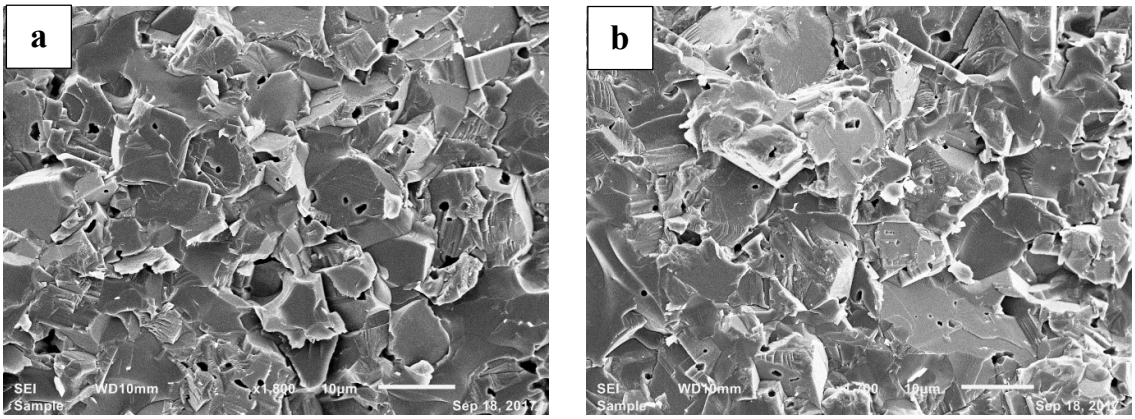

Figure 3.3: SEM micrographs of: (a) M3 MMA manifold; (b) M4 MMA manifold [14].

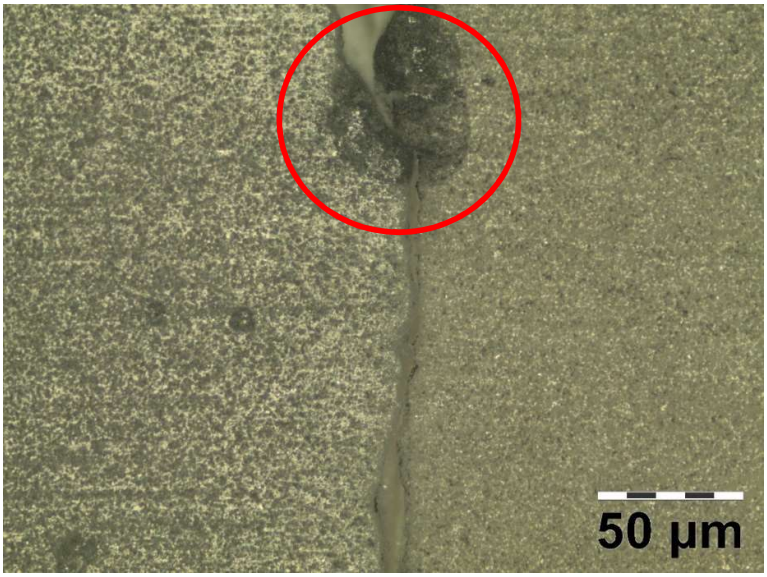

Figure 3.4: Optical micrograph of the tensile surface of failed M4 MMA manifold material indicating a surface pore acting as the origin of failure

Figure 3.4 depicts the surface pore of size 30 µm on the tensile surface of a M4 MMA manifold specimen which failed at a maximum flexural stress of 86 MPa at a loading rate of 0.09 mm/s, the lowest value of the batch. The large surface pore on the tensile surface indicated in Figure 3.4 was identified as the origin of failure for that specimen. Failures originating from

the large surface pores were also observed in other weak specimens in the same batch of M4 MMA manifold materials. Similar observations were made in the M4 manifold specimens loaded at rate of 0.00009 mm/s.

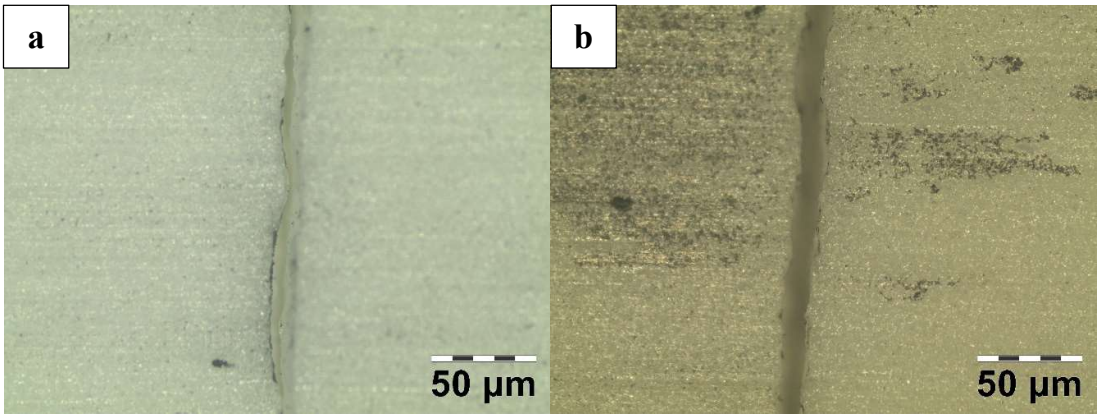

Figure 3.5: Optical micrograph of the tensile surface of M4 MMA manifold specimens which failed at a flexural stress of : (a) 204 MPa; (b) 162 MPa

Figure 3.5 depicts the fracture surfaces of specimens which failed at 204 MPa and 162 MPa at a loading rate of 0.09 mm/s, the highest and the median values in the batch respectively. No surface pore could be identified as the origin of failure on the tensile surface of both the specimens. Similar observations were made in the M4 manifold specimens loaded at rate of 0.00009 mm/s.

3.2 Porous MMA Tubes

The strength distributions of the Ceracomb tube material were evaluated at a loading rate of 0.009 mm/s under ambient conditions, 0.09 mm/s and 0.00009 mm/s at 850°C under extreme environmental conditions. Extreme environmental conditions for porous tubes was defined as 850°C with 50% moisture, 47.5% nitrogen and 2.5% hydrogen by volume. The SCG

of Ceracomb tubes was also studied at 850°C under the extreme environmental condition. These results were then compared with the properties of porous MMA tubes evaluated in the past [14].

3.2.1 Strength Distribution Analysis of Ceracomb Tube Material

Figure 3.6 depicts the flexural strength distribution of Ceracomb tube evaluated under ambient condition and at 850°C under extreme environmental condition. The values of the Weibull modulus, Modulus of Rupture (MoR) and stress range of both Ceracomb and porous MMA tube materials are listed in Table 3.3.

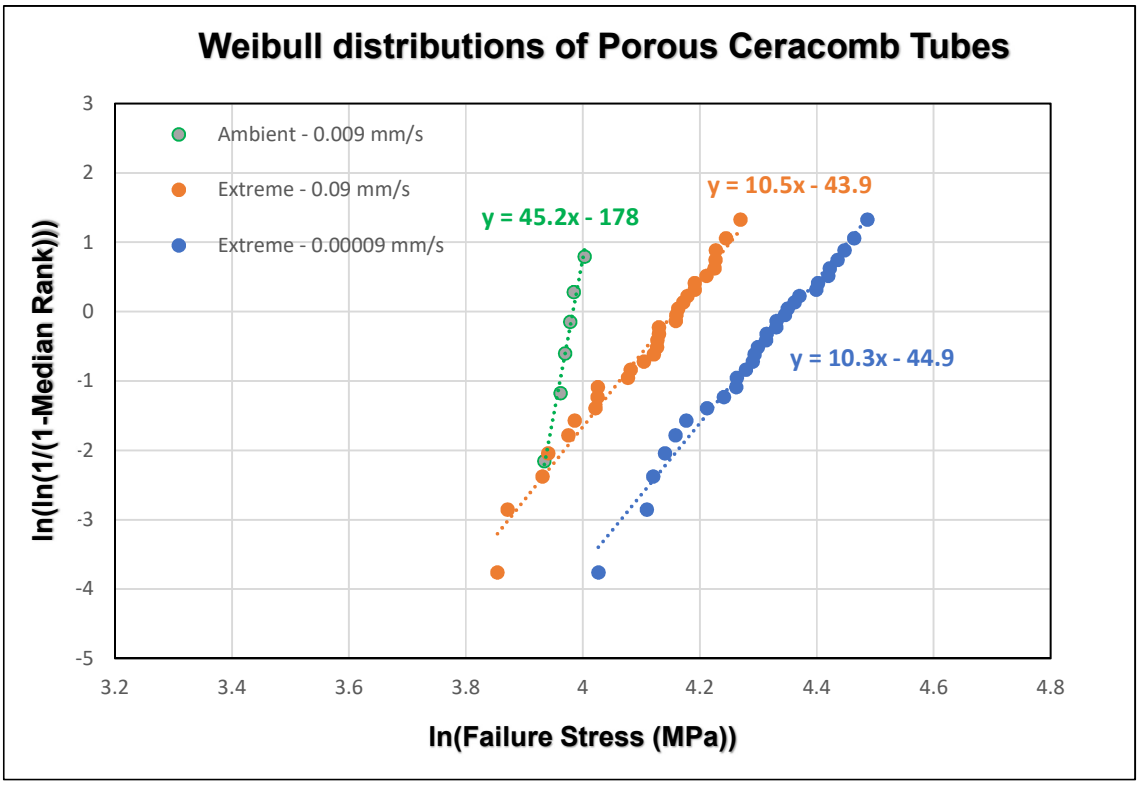

Figure 3.6: Weibull Plots of the porous Ceracomb tubes evaluated under ambient and 850°C under extreme environmental condition

The Weibull modulus of the Ceracomb tubes decreased from 45 to 10 when the testing conditions changed from 20°C in air to 850°C with 50% moisture, 47.5% nitrogen and 2.5% hydrogen by volume, indicating a drop in the consistency of flaws in material with the introduction of extreme environmental conditions. The modulus had minimal variation with the increase in the loading rate at 850°C under extreme environmental conditions. The MoR increased with the increase in the temperature and the introduction of moisture and gaseous mixture. The MoR decreased by 17%, from 78 MPa to 65 MPa when the loading rate was increased from 0.00009 mm/s to 0.09 mm/s.

It must be noted that only 6 tests were conducted at ambient conditions. Therefore, the values of the modulus and MoR evaluated at ambient conditions and hence the comparison of the same with the results from extreme environmental conditions tests may not be accurate.

Table 3.3: Comparison of Weibull parameters of Ceracomb and Porous MMA tubes evaluated at ambient and extreme environmental conditions

Material	**Loading Rate (mm/s)**	**Testing Conditions**	**m**	**MoR (MPa)**	**Average Stress (MPa)**	**Min Stress (MPa)**	**Max Stress (MPa)**
Ceracomb	0.009	Ambient	45.2	51.3	53.1	51.1	54.8
	0.09	Extreme	10.5	65.4	61.0	47.2	71.5
	0.00009	Extreme	10.3	78.2	74.3	56.1	88.8
Porous MMA [14]	0.009	Ambient	31.7	51.1	50.3	46.8	54.6
	0.09	Extreme	27.3	67.9	66.6	61.1	72.4
	0.00009	Extreme	24.6	69.6	68.1	62.0	75.2

The Weibull modulus for the porous MMA tubes had decreased from 32 to 27 when the testing conditions changed from 20°C in air to 850°C with 50% moisture, 47.5% nitrogen and 2.5% hydrogen by volume [14], like what was observed in the Ceracomb tubes. The MoR decreased with introduction of the extreme environment. There was little or no variation in the MoR with loading rate under extreme environmental conditions for the porous MMA tube material.

At the ambient conditions, the Ceracomb tubes had higher Weibull modulus than the porous MMA tubes. The Ceracomb tube evaluated at 850°C under extreme environmental conditions at 0.00009 mm/s yielded the highest MoR and fracture strength of the two materials. Porous MMA tubes had higher Weibull modulus than the Ceracomb tubes at 850°C under extreme environmental conditions indicating that the porous MMA tubes are more reliable than the Ceracomb tubes under that environment.

3.2.2 Slow Crack Growth Analysis of Ceracomb Tubes

Figure 3.7 depicts the slow crack growth response of Ceracomb tubes at 850°C with 50% moisture, 47.5% nitrogen and 2.5% hydrogen by volume. The material had a SCG coefficient of 64.7 MPa and an SCG exponent of -33.4. The low value of the SCG exponent implies that the material is very susceptible to slow crack growth at 850°C with 50% moisture, 47.5% nitrogen and 2.5% hydrogen by volume. The negative value of the SCG exponent implies that the flexural strength of the material decreases with the increase in the loading rate.

Table 3.4: Comparison of SCG properties of Ceracomb and porous MMA tube materials

Material	SCG Coefficient 'D'(MPa)	SCG Exponent 'n'
Ceracomb	64.7	-33.4
Porous MMA [14]	57.9	-218.4

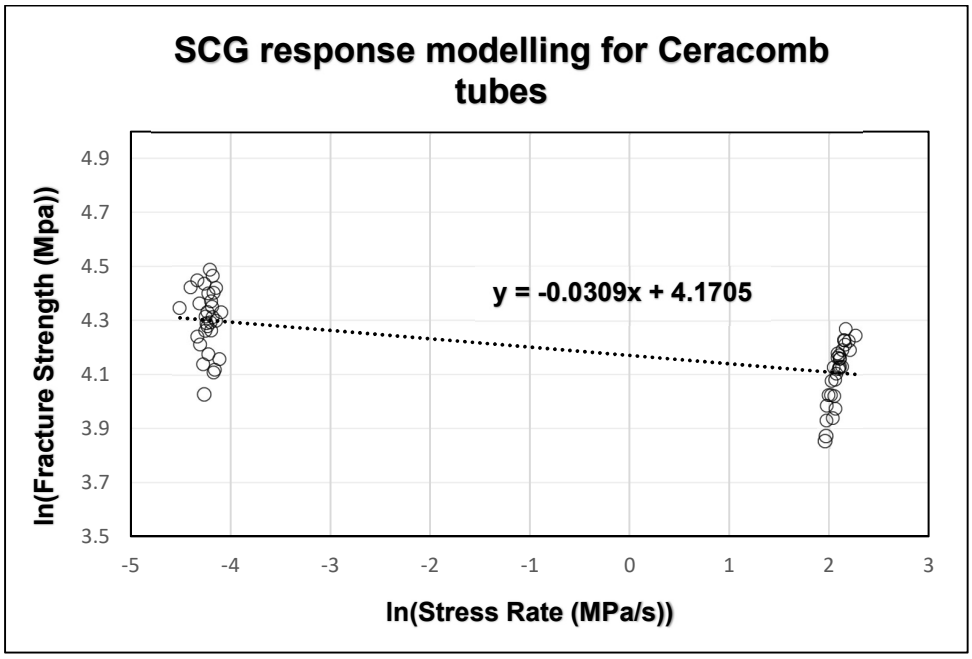

Figure 3.7: SCG response of Ceracomb tube under extreme environment.

As evident from the

Table 3.4, the porous MMA tube material had an SCG exponent of -218.4, which is substantially greater in magnitude than that of Ceracomb tube material, implying that porous MMA tube material resisted slow crack growth much better than the Ceracomb tube material. Porous MMA had lower SCG coefficient than Ceracomb tube implying that porous MMA had higher fracture toughness.

Radial lines were visible to the naked eye originating from the tensile surface of the weaker specimens, indicating that the fracture originated from the surface pores or flaws at this surface. Nevertheless, due to the large degree of porosity and high surface roughness, a proper fractographic analysis of the porous MMA tube materials could not be conducted.

3.3 Thermally Cycled Dense MMA Manifolds

Four-point-1/4-point flexural tests were performed on the thermally cycled M3 and M4 manifold materials at a loading rate of 0.009 mm/s under the ambient conditions to study the strength distributions. The strength distributions of thermally cycled M3 MMA manifold materials were evaluated at the loading rates of 0.09 mm/s and 0.00009 mm/s at 50°C and at 3.5% moisture by volume. The slow crack growth behavior of thermally cycled M3 MMA manifold material was also evaluated at 50°C and 3.5% moisture by volume.

3.3.1 Strength Distributions of Thermally Cycled M3 and M4 Manifolds

Figure 3.8 and Figure 3.9 are the Weibull plots of the strength distributions of thermally cycled M4 and M3 MMA manifold materials evaluated at a loading rate of 0.09 mm/s under the ambient conditions. The Weibull parameters for the thermally cycled M3 and M4 MMA manifold materials are listed in Table 3.5.

The Weibull modulus of the M4 MMA manifold material increased from 4 for 1 thermal cycle to 15 for 10 thermal cycles, indicating that the material became more reliable with the increase in the number of thermal cycles. The MoR of 137 MPa was the highest for M4 MMA material which underwent 5 thermal cycles. The MoR was similar for M4 MMA

material which underwent 1 and 10 thermal cycles respectively. Thus, 5 thermal cycles achieved the highest MoR for M4 MMA manifold material and M4 MMA manifold material which underwent 10 thermal cycles was the most reliable.

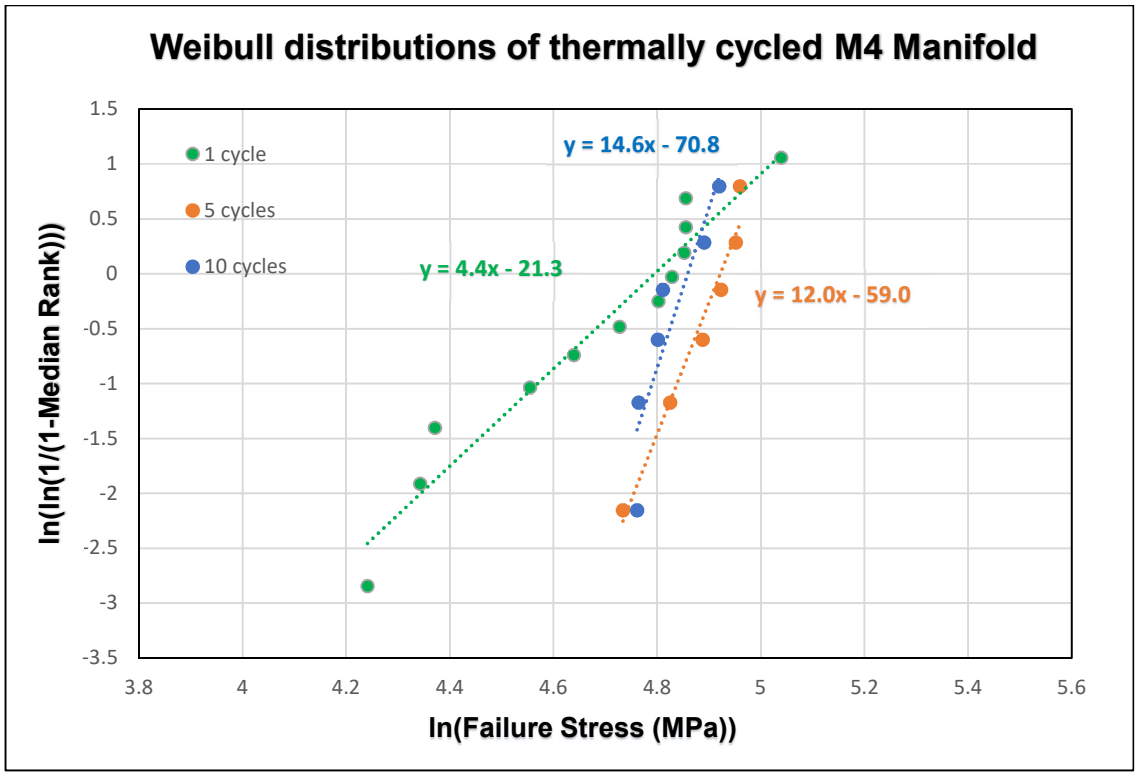

Figure 3.8: Weibull Plots of thermally cycled M4 MMA manifold materials evaluated at a loading rate of 0.009 mm/s under ambient conditions.

The M3 MMA manifold material that underwent 5 thermal cycles had a Weibull modulus of 4 and a MoR of 116 MPa. Both of these properties had lower values than those of the M4 MMA manifold material that underwent 5 thermal cycles, implying that the thermally cycled (5 cycles) M4 MMA manifold material is a better option than the thermally cycled (5 cycles) M3 MMA manifold material both in terms of the mechanical reliability and strength.

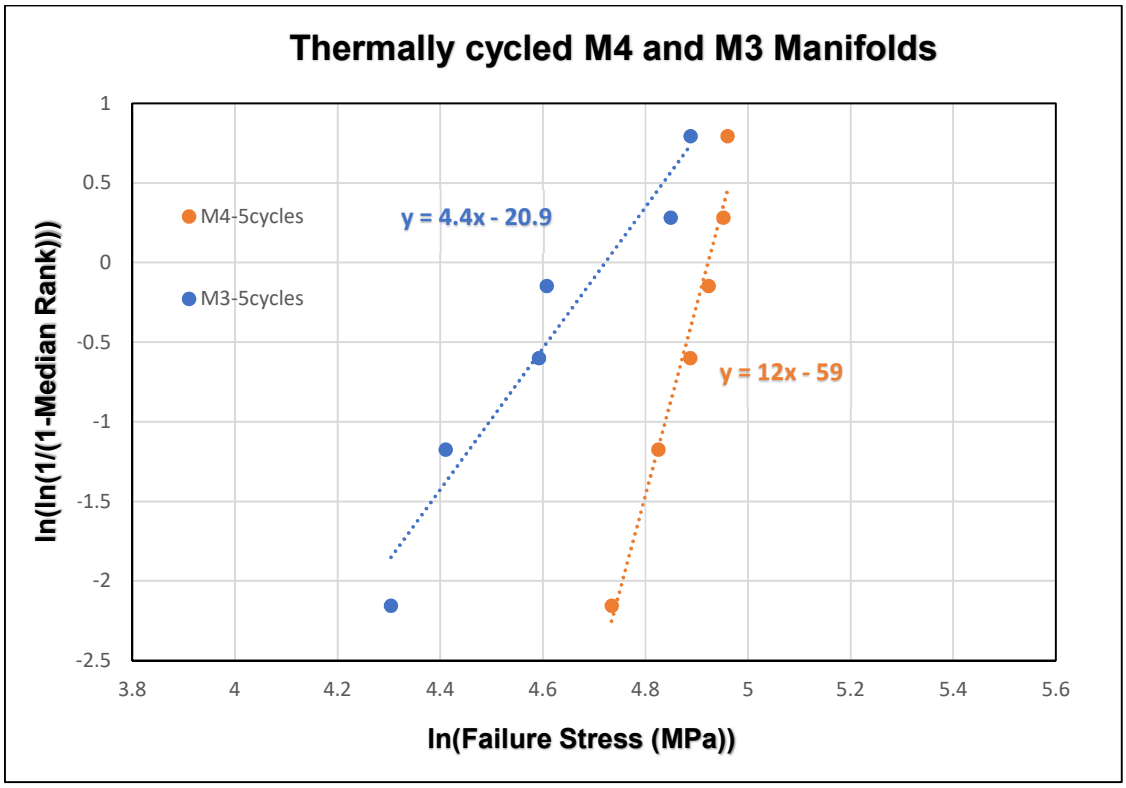

Figure 3.9: Weibull Plots of the thermally cycled (5 cycles) M3 and M4 MMA manifold materials evaluated at a loading rate of 0.009 mm/s under ambient conditions

Table 3.5: Weibull properties of the thermally cycled M3 and M4 manifold materials evaluated at a loading rate of 0.09 mm/s under ambient conditions.

Material	Number of Thermal cycles	m	MoR (MPa)	Average Stress (MPa)	Min Stress (MPa)	Max Stress (MPa)
M4	1	4.4	126.6	110.2	69.5	154.3
	5	12.0	136.5	132.1	113.8	142.6
	10	14.6	127.7	124.8	116.9	137.0
M3	5	4.4	115.6	102.6	74.0	132.7

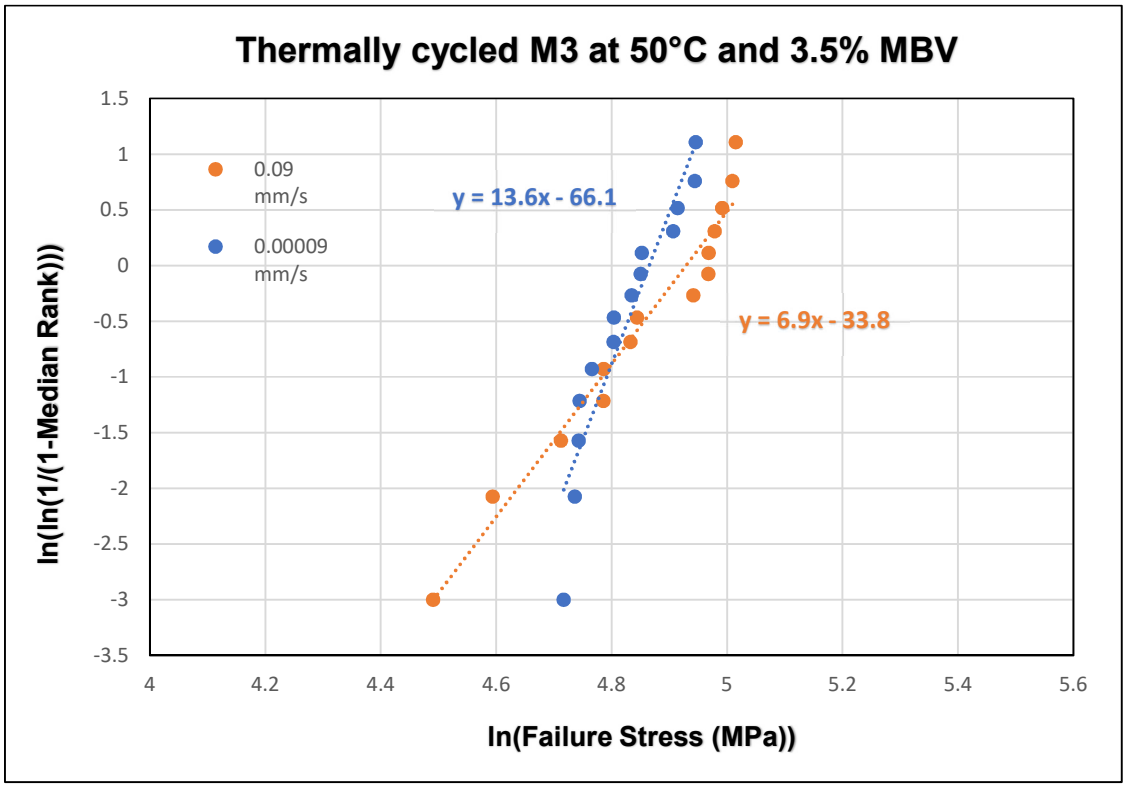

Figure 3.10: Weibull plots of the thermally cycled M3 MMA manifold material evaluated at 50°C and 3.5% moisture by volume

The Weibull modulus of thermally cycled (5 cycles) M3 MMA manifold material decreased from 14 to 6 with the increase in loading rate from 0.00009 mm/s to 0.09 mm/s, implying that the thermally cycled M3 MMA manifold material is more reliable at the lower loading rates. There was a small increase of 4% in the MoR and average failure stress of the thermally cycled M3 MMA manifold material when the loading rate was increased from 0.00009 mm/s to 0.09 mm/s. Therefore, the loading rate had minimal effect on the MoR of thermally cycled M3 MMA manifold material.

Table 3.6: Weibull properties of the thermally cycled M3 MMA manifold material and M3 MMA manifold material without any thermal cycling evaluated at 50°C and 3.5% moisture by volume

Material	Loading Rate (mm/s)	m	MoR (MPa)	Average Stress (MPa)	Min Stress (MPa)	Max Stress (MPa)
Thermally cycled M3	0.09	6.9	134.1	129.4	89.2	150.6
	0.00009	13.6	129.1	125.0	111.8	140.5
M3[14]	0.09	20.3	161.4	156.6	137.2	170.0
	0.00009	14.4	149.4	144.2	116.9	163.0

As evident from the Table 3.6, the M3 MMA manifold material without any thermal cycling had better Weibull modulus and the MoR than the thermally cycled M3 MMA manifold material. The Weibull modulus of the M3 MMA manifold material without any thermal cycling increased with the increase in the loading rate unlike the thermally cycled M3 MMA manifold material. The trend in variation of MoR with loading rate was similar for both the materials. Overall, thermal cycling M3 MMA manifold material 5 times resulted in a reduction of the Weibull modulus and MoR of the material, suggesting that the cycling makes the MMA manifold material less reliable and also reduces its strength.

3.3.2 Slow Crack Growth Analysis of Thermally Cycled M3 MMA Manifold

Figure 3.11 represents the slow crack growth response of the M3 MMA manifold material which underwent 5 thermal cycles evaluated at 50°C and 3.5% moisture by volume.

The values of the SCG properties of the thermally cycled (5 cycles) M3 MMA manifold material are listed in the Table 3.7.

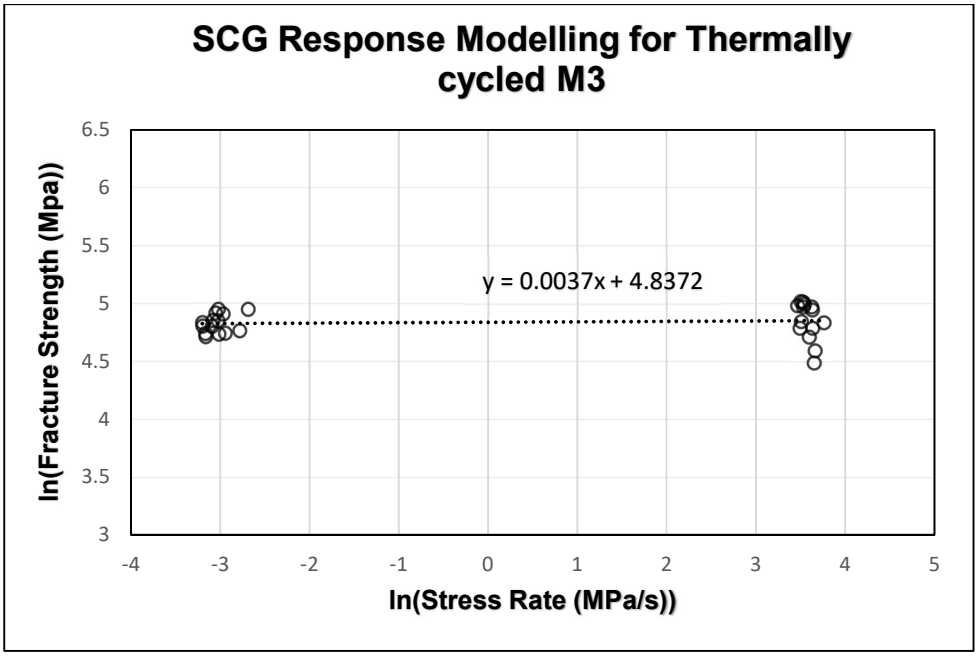

Figure 3.11: SCG response of the thermally cycled M3 MMA manifold material evaluated at 50°C and 3.5% moisture by volume

The thermally cycled M3 MMA manifold material had an SCG exponent of 269, implying that the loading rate had limited effect on the slow crack growth. Without any thermal cycling, the M3 MMA manifold had an SCG exponent of 81.6, implying that the thermal cycling slightly improved its resistance to fracture by slow crack growth. The SCG coefficient of M3 MMA manifold material decreased from 149 MPa to 126 MPa after thermal cycling, reducing its fracture resistance at 50^0C and 3.5% moisture by volume. Overall, the thermal cycling of the M3 MMA manifold material caused a reduction in the strength of the material but made it more resistant to the slow crack growth failure.

Table 3.7: Comparison of SCG properties of the thermally cycled M3 and M3 without any thermal cycling evaluated at 50°C and 3.5% moisture by volume

Material	SCG Coefficient 'D'(MPa)	SCG Exponent 'n'
Thermally cycled M3	126.1	269.3
M3 [14]	149.1	81.6

3.3.3 Optical Micrographs of Thermally Cycled M4 MMA Manifold Material

Figure 3.12 depicts the surface of the thermally cycled M4 MMA manifold materials. Surface microcracks and pores were visible on all the specimens. As evident from the Figure 3.12, the microcrack network grew with thermal cycling. The number of microcracks were the least in the M4 MMA manifold material which underwent a single thermal cycle (Figure 3.12(a)). The highest degree of microcracking was observed in the M4 MMA manifold material, which underwent 10 thermal cycles (Figure 3.12(c)). Small pores were visible on the surface of the M4 MMA manifold materials which underwent 1, 5 and 10 thermal cycles.

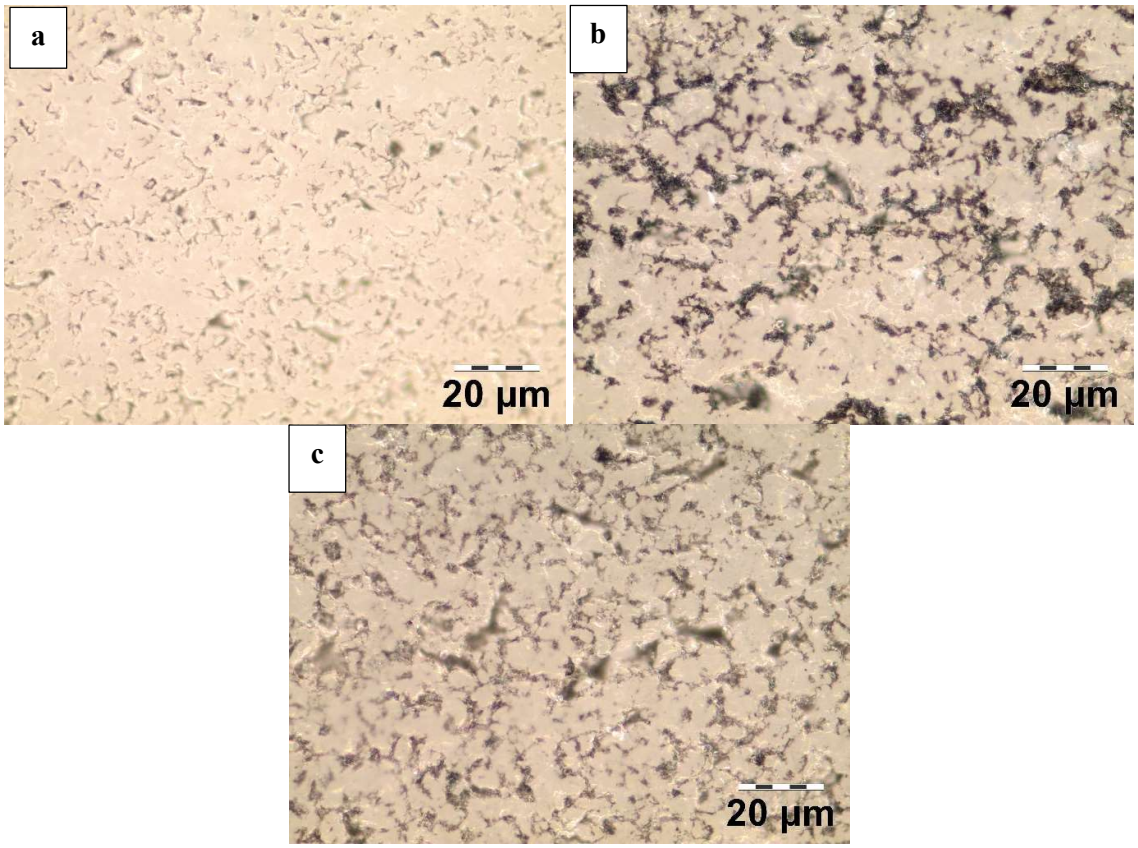

Figure 3.12: Optical micrographs (50x) of the surface of M4 MMA manifold material that underwent (a) 1 thermal cycle ; (b) 5 thermal cycles; (c) 10 thermal cycles

3.4 Thermally Cycled Porous MMA Tubes

Four-point-1/4-point flexural tests were performed on the thermally cycled porous MMA tube materials at a loading rate of 0.009 mm/s under the ambient conditions to study the strength distributions. Porous MMA tube materials were thermally cycled at five different conditions, viz., thermal cycling for 5 and 10 cycles at a cooling rate 5.33°C/min and soaking period of 2 hours, thermal cycling for 5 cycles with soaking period of 2 hours at cooling rates of 2.31°C/min and 8.89°C/min, thermal cycling for 5 cycling at a cooling rate of 2.31°C/min and soaking period of 6 hours.

The effect of the number of thermal cycling, cooling rate and soaking period on the strength distribution and reliability of the porous MMA tube material were evaluated. The Weibull properties of the porous MMA tube material which underwent aforementioned thermal cycles are listed in Table 3.8.

Table 3.8: Weibull properties of the thermally cycled porous MMA tubes evaluated under ambient conditions at a loading rate of 0.009 mm/s

Number of cycles	Cooling rate (°C/min)	Soaking period (hours)	m	MoR (MPa)	Average Stress (MPa)	Min Stress (MPa)	Max Stress (MPa)
0	0	0	31.7	51.1	50.3	46.8	54.6
5	5.33	2	23.3	53.7	52.5	49.6	55
10	5.33	2	18.6	54.3	52.6	48.9	56.7
5	2.31	2	21.4	51.6	50.9	48.3	54.1
5	8.89	2	33.2	53.9	53.4	51.4	55.3
5	2.31	6	13.7	54.2	51.8	47	57.4

Figure 3.13 represents the Weibull distribution of thermally cycled porous MMA tube material which underwent 5 thermal cycles at various cooling rates, evaluated under ambient conditions at a loading rate of 0.09 mm/s. As evident from Figure 3.13 and Table 3.8, the Weibull modulus of the porous MMA tube material increased from 21 to 33 when the cooling rate was increased from 2.31°C/min to 8.89°C/min, indicating that the material reliability increased when cooled at a faster rate. The Weibull modulus of the porous MMA tube material without any thermal cycling was 31.7, much greater than the thermally cycled porous MMA tube material cooled at a rate of 2.31°C/min and 5.33°C/min. But, the thermally cycled porous

MMA tube material cooled at a rate of 8.89°C/min, had a Weibull modulus of 33.2, which is approximately 5% greater than the same material without any heat treatment, indicating that thermal cycling with very rapid cooling rate can improve the reliability of the porous MMA tube material.

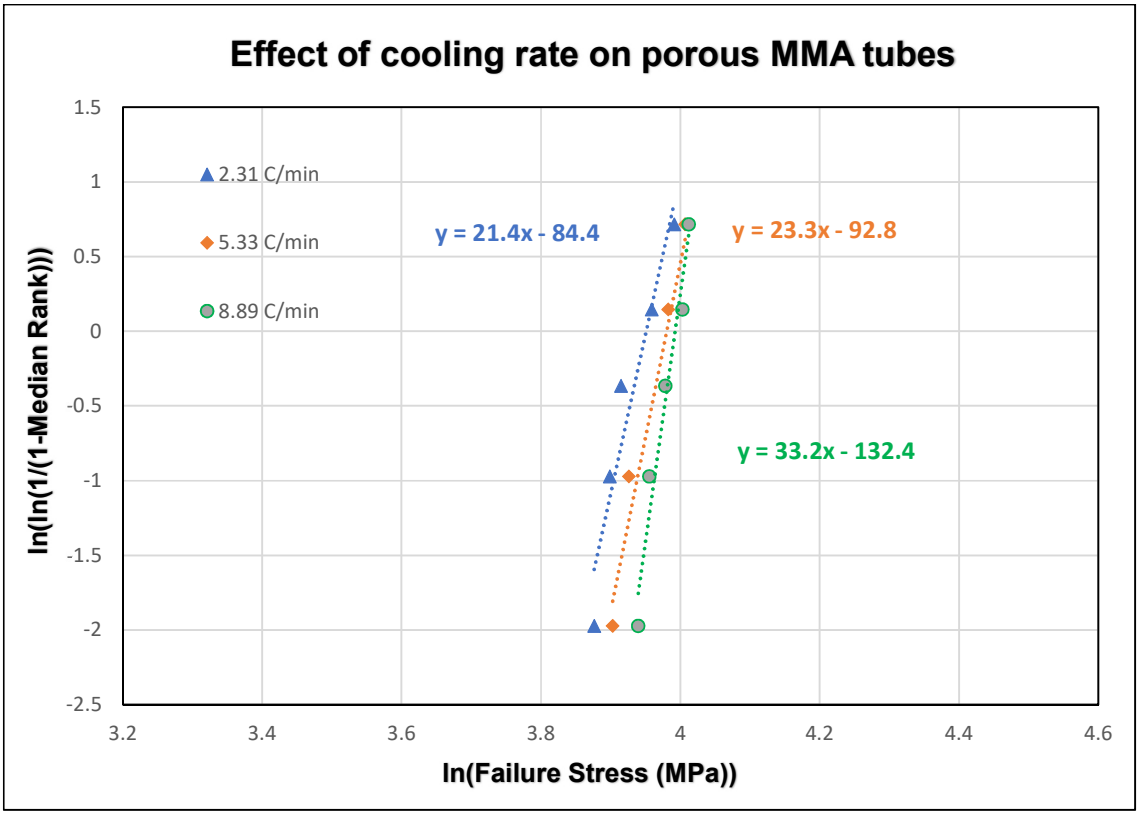

Figure 3.13: Weibull plots of the porous MMA tubes which underwent 5 thermal cycles at different cooling rates evaluated under ambient conditions at a loading rate of 0.009 mm/s

The MoR of the thermally cycled porous MMA tube material had limited variation, with MoR varying between 52 and 54 MPa (4% variation) when the cooling rate was increased from 2.31°C/min to 8.89°C/min. Therefore, the cooling rate has minimal effect on the MoR of the porous MMA tube material. The MoR of the materials sans heat treatment was 51, which was 2%-6% less than the thermally cycled porous MMA tubes, indicating that the thermal cycling causes no essential change in the strength and MoR of porous MMA tubes. It has to be

noted that the results presented may not be entirely accurate as only 5 samples were evaluated for each of thermally cycled group.

Figure 3.14 represents the strength distributions of the thermally cycled porous MMA tube materials soaked for 2 hours and 6 hours for 5 thermal cycles at a cooling rate of 2.31°C/min, evaluated under ambient conditions at a cooling rate of 0.009 mm/s.

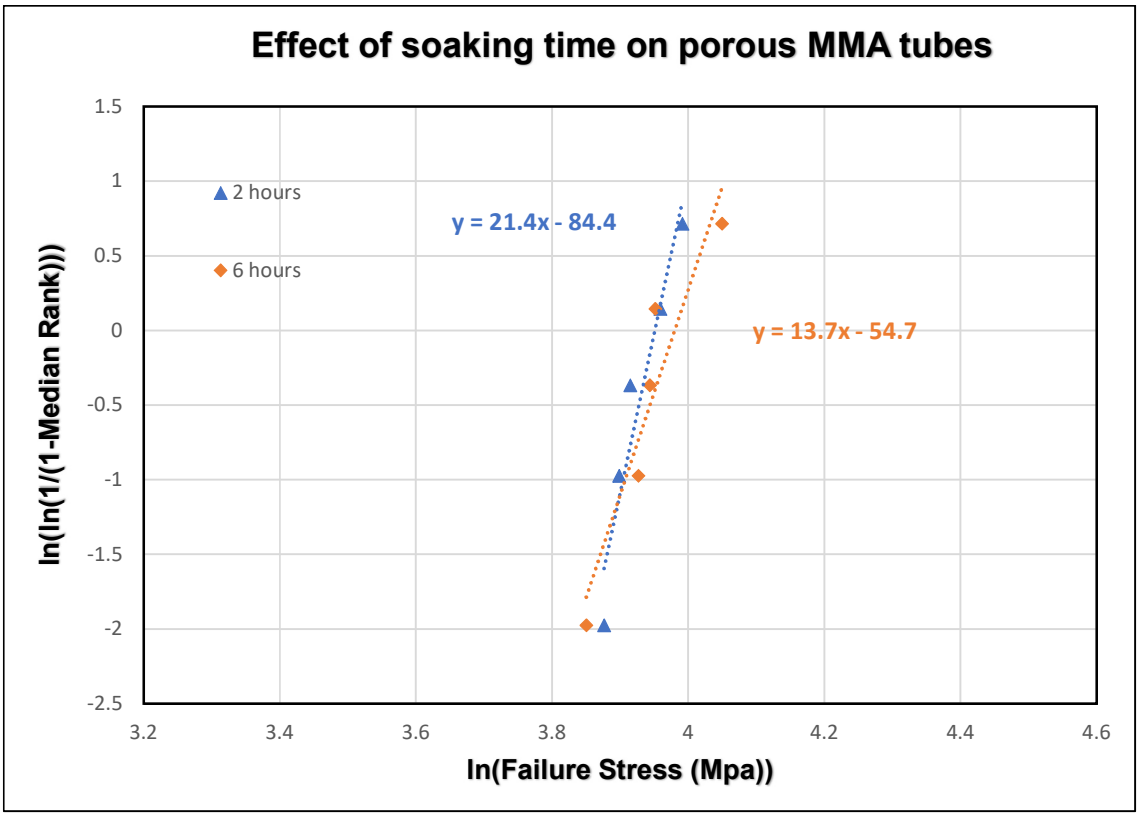

Figure 3.14: Weibull plots of the porous MMA tubes which underwent 5 thermal cycles with different soaking times evaluated under ambient conditions at a loading rate of 0.009 mm/s

As evident from the Figure 3.14 and Table 3.8, the Weibull modulus of the porous MMA tube material decreased by 33% from 21 to 14, when the soaking period was increased from 2 hours to 6 hours, indicating that the reliability of the material decreases when it is soaked at high temperatures and for long durations. The Weibull modulus of the porous MMA tube material without any thermal cycling was 31.7, which is much greater than the Weibull

modulus of the thermally cycled porous MMA tube material soaked for 2 hours and 6 hours. These results suggest that thermal cycling at a cooling rate of 2.31°C/min for 5 thermal cycles and for a soaking period greater than 2 hours drastically reduces the reliability of the material.

The soaking period had minimal effect on the MoR of the porous MMA tube material, with the MoR increasing by 4% from 52 MPa to 54 MPa when the soaking period was increased from 2 hours to 6 hours. The MoR of porous MMA tube without any heat treatment was 51, which was 2%-6% less than the thermally cycled porous MMA tubes of various soaking periods, indicating that the thermal cycling with any soaking period makes negligible improvement in the strength and the MoR of the porous MMA tubes. It has to be noted that the results presented may not be entirely accurate as only 5 samples were evaluated for each of thermally cycled group.

Figure 3.15 presents the strength distributions of the thermally cycled porous MMA tube materials soaked for 2 hours and cooled at a rate of 2.31°C/min for 5 and 10 thermal cycles, evaluated under ambient conditions at a cooling rate of 0.009 mm/s. As evident from the Figure 3.15 and the Table 3.8, the Weibull modulus of the porous MMA tube material decreased by 17% from 23 to 19, when the number of thermal cycles was increased from 5 to 10, indicating that the reliability of the material decreases with the increase in the number of thermal cycles. The Weibull modulus of the porous MMA tube material without any thermal cycling was 31.7, much greater than the Weibull modulus of the thermally cycled porous MMA tube material which underwent 5 and 10 thermal cycles, indicating that thermal cycling at a cooling rate of 2.31°C/min for soaking period of 2 hours for more than 5 cycles drastically impacts the reliability of the material.

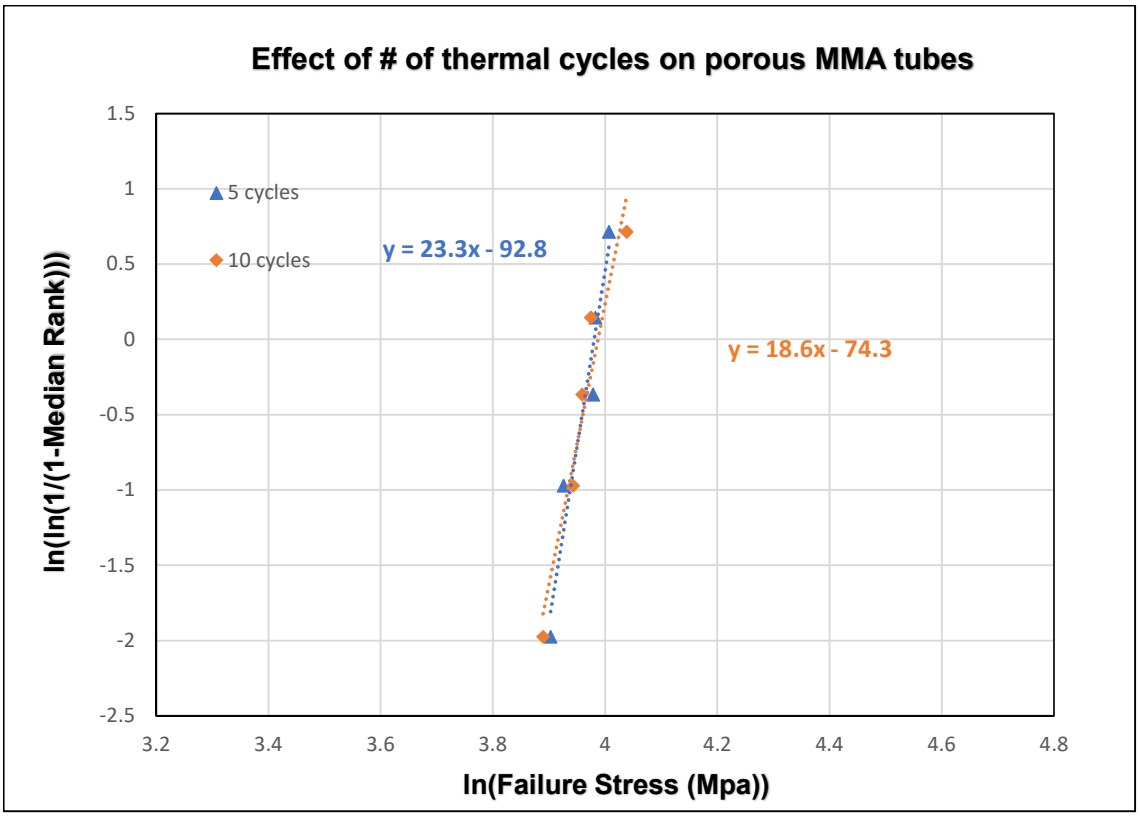

Figure 3.15: Weibull plots of the porous MMA tubes which underwent 5 and 10 thermal cycles with soaking period of 2 hours and cooled at a rate of 5.33°C/min, evaluated under ambient conditions at a loading rate of 0.009 mm/s

The change in the number of cycles had minimal effect on the MoR of porous MMA tube material, with the MoR increasing by 2% from 53 MPa to 54 MPa when the number of cycles was increased from 5 to 10. The MoR of the porous MMA tube without any heat treatment was 51, which was 4% and 6% less than the thermally cycled porous MMA tubes which underwent 5 and 10 thermal cycles respectively, indicating that the thermal cycling makes slight improvement in the strength and MoR of the porous MMA tubes. It has to be noted that the results presented may not be entirely accurate as only 5 samples were evaluated for each of thermally cycled group.

It can also be observed from the Table 3.8, that the porous MMA tube material cycled with the fastest cooling rate had the highest Weibull modulus. The porous MMA tube material which had greatest soaking period and the porous MMA tube material which was cycled the maximum number of times had the highest MoR and the samples from these two groups also achieved the highest fracture strength.

3.5 Evaluation of the Effect of Creep on Strength Distribution of Porous MMA Tubes

Figure 3.16 presents the flexural strength distributions of the porous MMA tube materials evaluated at 850°C and 50% moisture by volume, post creep at 850°C and 50% moisture by volume for 24 hours. The values of Weibull properties of the same are listed in Table *3.9*.

Table 3.9: Weibull properties of healed/creeped porous MMA tubes evaluated at 850°C and 50% moisture by volume at a loading rate of 0.009 mm/s

Loading condition	**m**	**MoR (MPa)**	**Average Stress (MPa)**	**Min Stress (MPa)**	**Max Stress (MPa)**
None	21.9	70.5	68.9	63.2	76.1
0.7 MPa for 24 hours (1% of MoR)	10.8	77.6	73.8	67.6	82.1
36 MPa for 24 hours (50% of MoR)	11.4	74.1	71.2	66.2	79.5

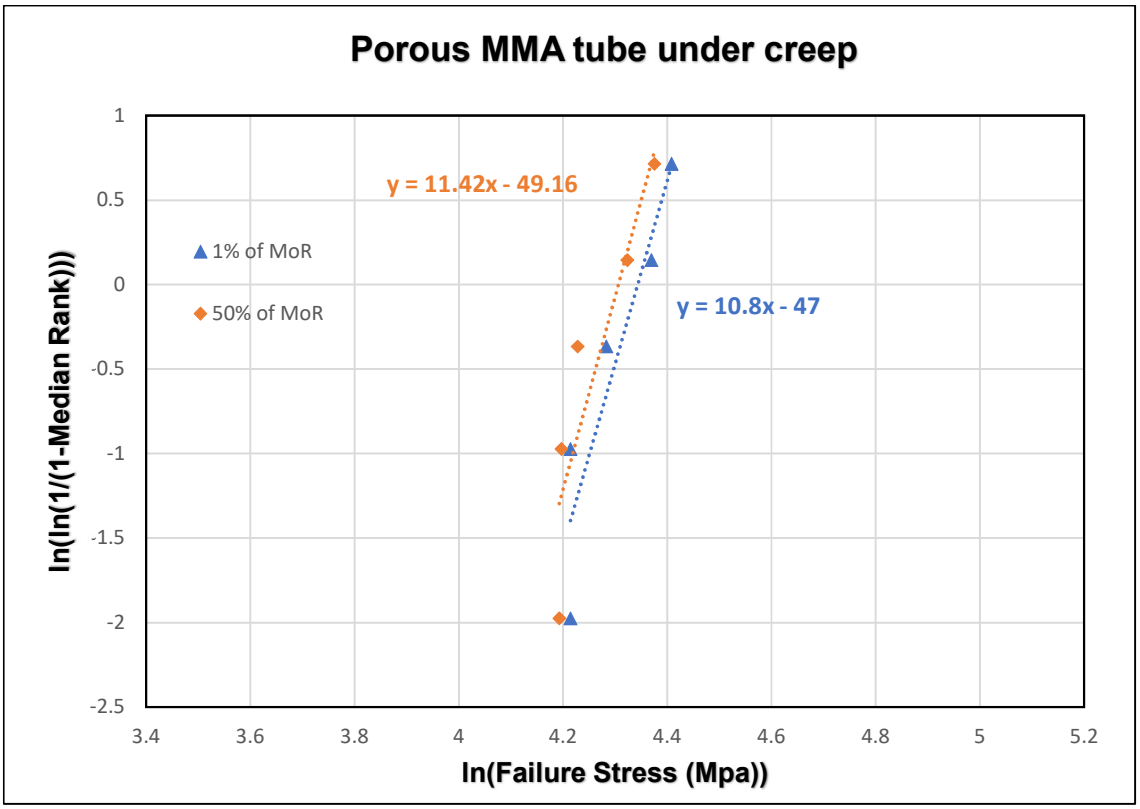

Figure 3.16: Weibull plots of porous MMA tube material evaluated at 850°C under an environment consisting of 50% moisture, 47.5% nitrogen and 2.5% hydrogen by volume , post holding the material at a particular stress for 24 hours

As evident from the Figure 3.16 and the Table *3.9*, the Weibull modulus of porous MMA tube material decreased by 51% and 48% when the material was loaded for 24 hours at 850°C and 50% moisture by volume for 0.7 MPa and 36 MPa respectively, implying that Weibull modulus of this material decreases with long exposure to extreme environmental conditions under stress.

The MoR of the porous MMA tube material increased by 10% and 4%, when the material was loaded at 0.7 MPa and 36 MPa respectively, for 24 hours at 850°C and 50% moisture by volume. This result suggests that the porous MMA tube material strength increases with exposure to extreme operational conditions under stress for longer duration.

The MoR of porous MMA tube material decreased by 5% from 78 MPa to 74 MPa, when loading stress for 24 hours at 850°C and 50% moisture by volume was increased from 0.7 MPa to 36 MPa. Thus, the strength of the porous MMA tube material does not appear to be influenced by prolonged loading at SOFC operational conditions. It has to be noted that only 5 samples were evaluated for both the groups. Therefore, the values of the modulus and MoR evaluated at ambient conditions and hence the comparison of the same with the results from extreme environmental conditions tests may not be accurate.

CHAPTER 4 : DISCUSSION

The microstructure, strength distribution and slow crack growth responses of the dense manifolds and porous tubes of MMA were evaluated in the as received condition and after thermal cycling. These evaluations were performed at a wide range of temperatures, moisture levels, and gas mixtures to mimic the operational conditions of SOFCs. These evaluations of MMA, a candidate SOFC material, at a wide range of SOFC operational environments is unprecedented and hence the results will be a good contribution to the literature.

Most of the literature reporting on the mechanical property evaluations are conducted either at ambient conditions or at high temperatures in air and sometimes with moisture or with inert gases. Therefore, the testing conducted for this work is unique, which will help provide a better understand the material behaviour at operating conditions and, hence, support the design of improved components for commercial systems.

4.1 Dense MMA Manifold

The M3 and M4 MMA manifold materials were evaluated at 50°C and 3.5% moisture by volume. The MoR of M4 MMA manifold material increased by 55 MPa (50%) when the loading rate was increased from 0.00009 mm/s to 0.09 mm/s. The failure stress ranged between 88 MPa and 124 MPa (range of 36 MPa) at slow loading rate and 126 MPa and 196 MPa (range of 70 MPa) at the fast loading rate, implying that the resistance to crack growth of the material improved with the increase in the loading rate. It must be noted that the strongest sample at the slow loading rate had lower fracture strength than the weakest sample at the fast loading rate.

It was also observed that the Weibull modulus of the M4 MMA manifold material decreased by approximately 7%, from 11.5 to 10.7 when the loading rate increased from 0.00009 mm/s to 0.09 mm/s, implying that the material had higher mechanical reliability at the slow loading rate than the fast loading rate. As evident from Figure 3.1, the weakest two samples loaded at 0.09 mm/s had fracture stress significantly lower than the other samples. The four weakest samples loaded at 0.00009 mm/s also had significantly lower fracture stress than the other samples. The material would have had higher Weibull modulus and hence be more reliable if not for these outliers. All of the weaker samples mentioned above had large surface pores on the tensile surface which acted the origin of failure. As these would be part of the systems that would be used for commercial purposes, it is important to modify the manufacturing processes of the components to ensure that the components made from the candidate MMA material would be more reliable.

It was evident from the optical micrographs of the fractured M4 MMA manifold specimens that the large surface pores which size greater than 30 microns on the tensile surface was the origin of failure in the weaker specimens of both the batches evaluated. Large surface pores could not be located and identified as the origins of failure in the samples with median and highest fracture strengths. From the fracture surface of the evaluated samples (not shown), it was evident that the fracture did not originate from the tensile surface in the samples with median and highest strength in both the batches. Hence, the large surface pores on the M4 MMA manifold material leads to premature failure of the material and also decreases its reliability.

The grain size was measured from the scanning electron micrographs of the M3 and M4 MMA manifold materials shown in Figure 3.3. The grain size of M3 manifold material ranged between 9 and 13 microns. M4 manifold material had grain size ranging between 10

and 21 microns. From the Table 3.1, it is evident that M3 had higher Weibull modulus than the M4 MMA material at both the loading rates, with the value being almost double at 0.09 mm/s, implying that the increase in the grain size of MMA manifold reduces the Weibull modulus and hence the reliability of the material. At the slow loading rate, M3 manifold material had a MoR of 149, 39 MPa higher than that of M4 at the same loading rate. At the fast loading rate, M3 and M4 had similar MoR, 161 MPa and 165 MPa respectively. This indicates that the grain size has significant influence of the strength of MMA manifold material at slow loading rate and has little or no effect on the strength of MMA manifold material at faster loading rate, when evaluated at 50°C and 3.5% moisture by volume.

The M4 MMA manifold material evaluated at 50°C and 3.5% moisture by volume, showed a very high rate dependence. From the SCG power law, M4 MMA manifold material was found to have an SCG exponent of 17 and an SCG coefficient of 126 MPa. The low value of SCG exponent indicates very high influence of loading rate on the slow crack growth which is very concerning. M3 MMA manifold material on the other hand an SCG exponent of 82 and SCG coefficient of 149 MPa. M3 had lower susceptible to slow crack growth compared to the M4 MMA manifold material. The SCG coefficient of M3 was 23 MPa greater than that of M4 MMA manifold component, indicating that the fracture toughness of M3 was greater than the fracture toughness of M4 MMA manifold material. This indicates that the increase in grain size makes the MMA manifold material more susceptible to slow crack growth failures and also reduces the fracture toughness of the material. Thus, having finer grains in the MMA manifold components is very important as it makes components stronger, improves reliability, fracture toughness and also the resistance to slow crack growth failures.

The Weibull modulus and the SCG exponents of various dense SOFC materials are listed in the Table 4.1 and Table 4.2 respectively. 3YSZ [56] had the highest Weibull modulus

at ambient conditions. 3YSZ [56] and dense MMA [14] had similar Weibull modulus at high temperatures under extreme environments. Dense MMA [14] and M3 MMA manifold materials were the top two materials in terms of SCG exponents, indicating better slow crack growth resistance than the other materials. Most of the materials reported were evaluated for slow crack growth at ambient conditions, and yet had lower SCG exponent values than the MMA materials which were evaluated at high temperatures and aggressive environments. Also, dense MMA [14] had a negative SCG exponent which wasn't the case in all the other dense SOFC materials reported. Negative value of SCG exponent 'n' indicates that the flexural strength increases with the reduction in the loading rate, which is suitable for long-term applications like SOFCs. Therefore, dense MMA, a candidate fuel cell material can be a really good choice for SOFC applications with its very low susceptibility to slow crack growth and good mechanical reliability at ambient and extreme operating conditions.

Table 4.1: List of the Weibull modulus of various dense SOFC materials

Sl. No	**Material**	**Environmental conditions**	**Weibull modulus (m)**	**Reference**
1	YSZ with 9.6 mol% of Yttria	Ambient	5.6	[54]
2		1000°C	6.2	
3	3YSZ	Ambient	31	[55]
4	6ScSZ	Ambient	19	
5	10-YSZ/30mol% alumina particulate composite	1000°C	4	[57]

6	10-YSZ/30mol% alumina platelet composite	1000°C	14	
7	10Sc1CeSZ	Ambient	11	[58]
8	3 YSZ	Ambient	20	
9	6Sc1CeSZ	Ambient	20	
10	6ScSZ	Ambient	18	
11	3 YSZ	850°C (80% Ar and 20% O_2)	20	[56]
12	6ScSZ	850°C (80% Ar and 20% O_2)	18	
13	Dense MMA	Ambient	20.7	[14]
14		850°C under 50% moisture, 2.5% hydrogen and 47.5% nitrogen by vol	19.4	
15	M3 MMA manifold	50°C under 3.5% MBV	20.3	
16	M4 MMA manifold	50°C under 3.5% MBV	11.5	Present work

Table 4.2: List of the SCG exponent of various dense SOFC materials

Sl. No	**Material**	**Environmental conditions**	**SCG exponent (n)**	**Reference**
1	YSZ with 9.6 mol% of Yttria	Ambient	16.6	[54]
2	10-YSZ	1000°C	8.3	[57]

3	10-YSZ/30mol% alumina particulate composite	1000°C	5.4	
4	10-YSZ/30mol% alumina platelet composite	1000°C	32.9	
5	6Sc1CeSZ	22°C in water	65	[58]
6	10Sc1CeSZ	92% MBV at 22°C	37	
7	6ScSZ	40% MBV at 22°C	54	
8		22°C in water	56	
9	3 YSZ	92% MBV at 22°C	55	
10		32% MBV at 22°C	54	
11	6ScSZ	250°C under inert environment	55	[56]
12		450°C under inert environment	26	
13	Dense MMA	850°C under 50% moisture, 2.5% hydrogen and 47.5% nitrogen by vol	-251	[14]
14	M3 MMA manifold	50°C under 3.5% MBV	82	
15	M4 MMA manifold	50°C under 3.5% MBV	16.9	Present work

4.2 Porous MMA Tubes

Porous MMA tube and porous Ceracomb tube materials were evaluated at ambient conditions and also at 850°C under an environment containing 50% moisture, 5% hydrogen and 45% nitrogen by volume. The MoR of porous Ceracomb tube material increased from 51 MPa at ambient conditions to 65 MPa and 78 MPa at 850°C under an environment containing 50% moisture, 5% hydrogen and 45% nitrogen by volume (extreme environment), implying that the MoR of the material increased with the increase in temperature and introduction of moisture and gas. Under the extreme environmental conditions, the MoR of porous Ceracomb tube material decreased by 16%, from 78 MPa to 65 MPa and the average fracture strength decreased from 74 MPa to 61 MPa, when the loading rate was increased from 0.00009 mm/s to 0.09 mm/s. The fracture strength ranged between 56 MPa and 89 MPa (range of 33 MPa) at the slow loading rate, between 47 MPa and 72 MPa (range of 25 MPa) at the fast loading rate, implying that the resistance to crack growth of the material declined with the increase in the loading rate.

The Weibull modulus of the porous Ceracomb tube material decreased by 77% from 45 to 10, when the conditions were changed from ambient environment to 850°C under extreme environment, implying that reliability of the material was extremely sensitive to the changes in temperature and corrosive environment. The reliability of the material decreased drastically on increase in temperature and exposure to humidity and gas. There was negligible variation in the Weibull modulus of the material at 850°C, when the loading rate was increased from 0.00009 mm/s to 0.009 mm/s. That implies that the loading rate has little or no effect on the reliability of porous Ceracomb tube material at 850°C under extreme environmental conditions. The high Weibull modulus of Ceracomb tube material at ambient conditions indicates that the failure origins in different specimens were similar, which would also mean the critical

porosity/flaw size and orientations were similar. The reduction in the value of Weibull modulus on introduction of high temperature and extreme environmental conditions indicates the large reduction in consistency of flaw size and orientation that was observed at ambient conditions. It must be noted that the samples were exposed to high temperatures and extreme environments for a very limited time period, therefore the effect of ageing or degradation of the material may not evident from the results presented in this section. Also, only 6 samples of porous Ceracomb tube were evaluated at ambient conditions, which is significantly less than the number of samples evaluated at other conditions. Thus, the results presented at ambient conditions may not be reliable and further work is suggested.

From the fractographic studies, it was found that the large pores on the tensile surface of the specimens act the origins of failures in the weaker samples in all the groups evaluated. Therefore, it is critical to ensure that pores and cracks are minimized to a large extent on the surface of the components manufactured from porous Ceracomb tube material, so that it could be utilized to build strong, fracture resistant and reliable commercial systems.

As evident from the Table 3.3, porous Ceracomb tube material had better Weibull modulus than porous MMA tube material at ambient conditions, and porous MMA tube material had better Weibull modulus at high temperature under extreme environmental conditions, implying that porous Ceracomb tube material is more reliable than the porous MMA tube material at ambient conditions. But, the Weibull modulus of porous MMA tube material was at least 52% greater than that of porous Ceracomb tube material at 850°C under extreme environmental conditions, implying that porous MMA tube material is more reliable at 850°C under extreme environmental conditions. The MoR of both the materials were similar at the ambient conditions. The MoR of the porous MMA tube material was 5% greater than the porous Ceracomb tube material at the fast loading rate, and the MoR of porous Ceracomb tube

material was 10% greater than the porous MMA tube material at the slow loading rate at 850°C under extreme environmental conditions.

The porous Ceracomb tube material evaluated at 850°C under an environment containing 50% moisture, 5% hydrogen and 45% nitrogen by volume, showed susceptibility to slow crack growth degradation. From the SCG power law, porous Ceracomb tube material was found to have an SCG exponent of -33 and an SCG coefficient of 65 MPa. The low value of SCG exponent indicates very high influence of loading rate on the slow crack growth which is very concerning. Porous MMA tube material on the other hand an SCG exponent of -218 and SCG coefficient of 58 MPa. Porous MMA tube material had very low susceptibility to slow crack growth failure, unlike porous Ceracomb tube material. The SCG coefficient of porous Ceracomb tube material was 11% greater than that of porous MMA tube material, indicating that porous Ceracomb tube material had greater fracture toughness than the porous MMA tube material at the high temperature and extreme environmental conditions. The negative value of SCG exponent of both the tube materials indicate that the flexural strength increases with the reduction in the loading rate, which is suitable for long-term applications like Solid Oxide Fuel Cells. The difference between the two porous tube materials is unknown to the author. Therefore, the reasons for the difference in mechanical performance between the two tube materials could not be discussed.

The Weibull modulus and the SCG exponents of various porous SOFC materials are listed in Table 4.3 and Table 4.4 respectively. Porous ceramic materials are generally used to fabricate electrodes, interconnects and tapes and also used as substrates for SOFCs. Most of the evaluation on the porous SOFC materials reported in literature contain evaluations of materials at room temperature and high temperatures in air. Very few papers were found on the evaluations of porous SOFC materials at high temperatures under gaseous or humid

environments [13]. As evident from the Table 4.3, the porous Ceracomb tube material and porous MMA tube materials are standout performers in reliability at ambient and extreme environmental conditions. Porous MMA tube material [14] and porous Ceracomb tube material were the best among the above reported material in slow crack growth behavior at high temperatures. Most of the materials reported were evaluated for slow crack growth at the ambient conditions, and yet had lower SCG exponent values than the porous MMA tube materials. Also, porous MMA/Ceracomb tube material had a negative SCG exponent unlike other porous SOFC materials reported. Negative value of SCG exponent 'n' indicates that the flexural strength increases with the reduction in the loading rate, which is suitable for long-term applications like Solid Oxide Fuel Cells. Therefore, porous MMA, a candidate fuel cell material can be a really good choice for SOFC applications with its very low susceptibility to slow crack growth and good mechanical reliability at ambient and operating conditions.

Table 4.3: List of the Weibull modulus of various porous SOFC materials

Sl. No	**Material**	**Environmental conditions**	**Weibull modulus (m)**	**Reference**
1	LSM	25°C in air	6.7	[59]
2		800°C in air	3.7	
3	GC-9	25°C in air	5.5	
4		800°C in air	6.0	
5	BSCF	Ambient	5	[60]
6	LSCF	Ambient	3	
7	CGO	Ambient	4	
8	Ni-3YSZ	Ambient	10.0	[61]

9	20 YDC	Ambient	3.6	
10	LaWO54-P30	Ambient	15	[62]
11	LaWO54-P32	Ambient	7.8	
12	LaWO54-P39	Ambient	9.4	
13	Porous MMA tube	Ambient	31.7	[14]
14		850°C under 50% moisture, 5% hydrogen and 45% nitrogen by vol	27.3	
15	Porous Ceracomb tube	Ambient	45.2	Present work
16		850°C under 50% moisture, 2.55% hydrogen and 47.5% nitrogen by vol	10.5	

Table 4.4: List of the SCG exponent of various porous SOFC materials

Sl. No	**Material**	**Environmental conditions**	**SCG exponent (n)**	**Reference**
1	Ni -YSZ (26%,34% & 40% porosity)	Ambient	18.9, 19.7, 20	[13]
2		600°C (4% H_2 and 96% Ar)	11.8, 12.6, 12.1	
3		800°C (4% H_2 and 96% Ar)	9.5, 10.9, 10.5	
4	BSCF	Ambient	83	[60]
5	CGO	Ambient	25	

6	Porous MMA tube	850°C under 50% moisture, 2.5% hydrogen and 47.5% nitrogen by vol	-218.4	[14]
7	Porous Ceracomb tube	850°C under 50% moisture, 2.5% hydrogen and 47.5% nitrogen by vol	-33.4	Present work

4.3 Thermal Cycling of Dense MMA Manifold

The M3 and M4 dense MMA manifold materials where thermally cycled for 1, 5 and 10 cycles. The flexural strength distribution of M3 and M4 dense MMA manifold materials were evaluated at a loading rate of 0.009 mm/s under ambient conditions. The slow crack growth response of the M3 MMA manifold material which underwent 5 thermal cycles was evaluated at 50°C and 3.5% moisture by volume.

The Weibull modulus of M4 MMA manifold increased by 232%, from 4 to 15, when the number of thermal cycles was increased from 1 to 10, implying that the reliability of the material increases with the increase in the number of thermal cycles. The MoR increased from 127 MPa to 137 MPa by 8%, when the number of thermal cycles was increased from 1 to 5. The MoR decreased from 137 MPa to 128 MPa by 7% when the number of thermal cycles was

increased from 5 to 10 cycles. There was little difference between the MoR of M4 MMA manifold material which underwent 1 and 10 thermal cycles, indicating that there was no clear variation in the MoR of the material with respect to the number of thermal cycles.

From the complimentary optical micrographic evaluations of the thermally cycled M4 MMA manifold materials, it was observed that the number of microcracks increased with the increase in the number of thermal cycles. The microcracks were developed on the surface of the M4 MMA manifold material due to repeated thermal shocks which exerted tensile stress on the samples. The microcrack network grew with the increase in the number of thermal cycles, implying that the reliability of M4 MMA manifold material improved with the increase in the number of microcracks and large microcrack network.

As evident from Table 3.5, the Weibull modulus and MoR of M4 MMA manifold material which underwent 5 thermal cycles were 63% and 15% greater, respectively, than those for the M3 MMA manifold material which underwent 5 thermal cycles. The change in the Weibull parameters signify a higher mechanical reliability and strength of thermally cycled M4 MMA manifold materials at ambient conditions. The M3 and M4 MMA manifold materials had grain size ranging between 9 and 13 microns, and 10 and 21 microns, respectively, before undergoing any thermal cycling. The grain structure of the two materials post thermal cycling were not evaluated. These results suggest that coarser grain structure perform better under thermal cycling and improve the reliability of dense MMA manifold materials. As the microstructure of these materials post thermal cycling couldn't be evaluated in the present study, the mechanism behind failures of these materials and the reasons for this behavior couldn't be evaluated.

As evident from Table 3.6, the Weibull modulus of M3 MMA manifold material, evaluated at 50°C and 3.5% MBV decreased by 66%, and 6% at a loading rate of 0.00009 mm/s

and 0.009 mm/s respectively after it underwent 5 thermal cycles. The MoR decreased by 17% and 14% at loading rates of 0.00009 mm/s and 0.009 mm/s, indicating that the thermal cycling of M3 MMA manifold material leads to reduction in reliability and strength.

From the slow crack growth evaluations of thermally cycled M3 MMA manifold material, it was found that the SCG exponent increased by 230%, from 82 to 269 on thermal cycling. The SCG coefficient decreased by 15% from 149 MPa to 126 MPa, implying that the thermal cycling which led to development of microcracks on the surface of M3 MMA manifold material, led to the drastic improvement in the resistance to slow crack growth degradation, but with substantial loss in the fracture toughness of the material.

The two phases of MMA, magnesia and magnesium aluminate have a coefficient of thermal expansions of 13.5 x 10^{-6} K^{-1} and 7.6 x 10^{-6} K^{-1}, respectively [47]. Due to the difference in the coefficient of thermal expansion between the two constitutive phases, high tensile stresses can develop at the micro level around inclusions or other defects during the cooling phase of a thermal cycle, which could promote microdamage or microcracking. This leads to accumulation of strain energy [42], which would likely improve the slow crack growth resistance of the material, and also improve the mechanical reliability of the material. It is evident from the aforementioned results and discussion that thermal cycling can be used to improve the reliability and slow crack growth behaviour of the dense MMA manifold materials. However, a compromise will have to be made in the fracture strength and fracture toughness of the material.

4.4 Thermal Cycling of Porous MMA Tubes

Thermally cycled porous MMA tubes were evaluated at a loading rate of 0.009 mm/s under ambient conditions. The effect of cooling rate, soaking time and the number of thermal cycles on the reliability and strength distribution of porous MMA tube material was studied. As evident from Table 3.8, the Weibull modulus of the thermally cycled porous MMA tube material decreased by 41% from 32 to 19, when the number of thermal cycles was increased from 0 to 10, implying that the flaw size and orientation in the material became less consistent with the increase in the number of thermal cycles, which leads to a reduction in the reliability of the material. The MoR increased marginally from 51 MPa to 54 MPa when the number of thermal cycles was increased from 0 to 10, implying that thermal cycling could potentially improve the strength of the porous MMA tube material. Though not evaluated and proven experimentally, the slight increase in the flexural strength post thermal cycling may be due to the formation of microcracks on the surface of the material. Again, this mechanistic behavior is expected in MMA due to differences in the coefficient in thermal expansion of the constitutive phases of MMA [43].

The Weibull modulus of the porous MMA tube increased by 55%, from 21.4 to 33.2, when the cooling rate was increased from 2.31°C/min to 8.89°C/min. That increase implies that the size distribution of flaws in the material became more consistent with the increase in cooling rate thereby leading to improvement in the mechanical reliability of porous MMA tube material. The MoR did not change (52 MPa to 54 MPa) when the cooling rate was increased from 2.31°C/min to 8.89°C/min, which suggests that the increase in cooling rate had negligible influence on the number of microcracks in the material, as reflected by the MoR of porous MMA tube material. The Weibull modulus of the porous MMA tube material decreased from 21 to 14 (by 36%) when the soaking period was increased from 2 hours to 6 hours, suggesting

a reduction in reliability. The MoR increased by 2 MPa when the soaking period was increased from 2 hours to 6 hours, indicating that exposure of the material to high temperatures for longer duration has essentially no effect on the strength of the porous MMA tube material.

Curzio et al. [38] evaluated the effect of thermal cycling on the mechanical properties and residual stresses in porous Ni-YSZ/YSZ bi-layer SOFC materials. The samples were thermally cycled between 20°C and 800°C, for 1, 25, 250 and 1250 cycles. They found that there was no significant change in the porosity and elastic modulus of Ni-YSZ/YSZ bi-layer materials with the number of thermal cycles. However, they reported that the MoR decreased by as much as 20% with thermal cycling. They also observed that residual stresses in the YSZ layer were compressive and underwent relaxation during the initial stages of thermal cycling and did not change significantly with thermal cycling beyond the initial stage. They also suggested that creep deformation of Ni-YSZ could be the dominant mechanism in the initial stages of thermal cycling at 800°C.

Choi and Bansal [63] evaluated the effect of thermal cycling on the mechanical properties of YSZ/30 mol% platelet alumina SOFC material. The thermal cycling was conducted with a heating rate of 10°C/min and a cooling rate of 20°C/min for 10 cycles between 200°C and 1000°C. They found that the flexural strength doesn't degrade with thermal cycling, indicating negligible influence of the difference in the coefficient of thermal expansion between the YSZ matrix and alumina grains.

It needs to be noted that the number of thermal cycles applied in evaluating the porous MMA tube material is far lower than it may be undergo in service. But, the behavior of the material was quite similar to the response of Ni-YSZ/YSZ bi-layer SOFC materials during the initial stages of thermal cycling at 800°C [38].

CHAPTER 5 : CONCLUSIONS

5.1 Conclusions

Experimental evaluations were conducted to evaluate the mechanical reliability, strength distributions and slow crack growth properties of dense MMA manifold and porous MMA tube materials in the as received condition and after thermally cycling. The evaluations of the dense MMA manifold materials were conducted at ambient conditions and at 50°C with 3.5% moisture by volume. The evaluations of the porous MMA tube materials were conducted at ambient conditions and at 850°C in an environment containing 50% moisture, 45% nitrogen and 5% hydrogen by volume. Evaluation of the flexure strength was conducted as per ASTM C1161 standard, and the strength distributions were evaluated by using the two parameter Weibull analysis to measure the Weibull modulus (m) and the Modulus of Rupture (MoR) of the materials. Constant stress rate slow crack growth evaluations at non ambient conditions were conducted as per ASTM C1368 to find the SCG properties, viz., SCG exponent and coefficient. The following conclusions were drawn from these evaluations:

1. There was minimal influence of the loading rate on the Weibull modulus of the dense MMA manifold material at 50°C with 3.5% moisture by volume. The values of 'm' were found be 11.5 and 10.7 at the loading rates of 0.00009 mm/s and 0.09 mm/s respectively. The MoR of the material increased with loading rate in this environment from 110 MPa to 165 MPa with increase in rate from 0.00009 mm/s to 0.09 mm/s. Using these results, the SCG exponent and coefficient were found to be 17 and 126 MPa, respectively, which indicates a reduction in the potential for slow crack growth failure with increasing loading rate.

2. At 50°C and 3.5% moisture by volume environment, the Weibull modulus, MoR and SCG exponent increased with a decrease in grain size for the dense MMA manifold material. The

MMA manifold material with grain size ranging between 9-13 microns had better Weibull modulus, MoR and SCG exponent than that of the MMA manifold material with grain sizes ranging between 10-21 microns.

3. For the porous MMA tube material, the Weibull modulus increased with temperature as the value of 'm' decreased from 45 at 20°C to 10 at 850°C. The MoR of the material also increased from 51 MPa at 20°C to 65 MPa and 78 MPa at 850°C at the loading rates of 0.09 mm/s and 0.00009 mm/s respectively. Loading rate had limited effect on the Weibull modulus and had detrimental effect on the MoR of the material at 850°C under extreme environmental conditions. The porous tube material exhibited high sensitivity to slow crack growth at 850°C and extreme environmental conditions, with an SCG exponent of -33 and SCG coefficient of 65 MPa.

4. The Weibull modulus of the MMA manifold material increased with thermal cycling from 4 after 1 thermal cycles to 15 after 10 thermal cycles. There was no trend in the MoR of the material with increasing thermal cycles. Thermal cycling reduced the Weibull modulus and MoR of the M3 MMA manifold material evaluated at 50°C with 3.5% moisture by volume. The values of 'm' decreased from 20 and 14 without thermal cycling to 7 and 14 after 5 thermal cycles. The values of 'MoR' decreased from 157 MPa and 144 MPa without thermal cycling to 129 MPa and 125 MPa after 5 thermal cycles. Furthermore, the slow crack growth resistance of the M3 MMA increased with thermal cycling from 82 without thermal cycling to 269 after 5 thermal cycles.

5. The influence of thermally cycling on the strength distribution of the porous MMA tubes was also evaluated. The Weibull modulus of the MMA tube increased with cooling rate from 21 at 2.31°C/min to 33 at 8.89°C/min. The Weibull modulus also decreased with increasing number of thermal cycles from 32 at 0 cycles to 23 at 5 cycles to 19 at 10 cycles. The Weibull

modulus also decreased with increasing thermal soak period from 32 at 0 hours to 21 at 2 hours to 14 at 6 hours. The MoR of the porous MMA tube material increased with all thermal treatments performed.

6. For all the evaluations conducted, it was found that large surface pores were the limiting factor in the reliability of these materials. Specifically, large surface pores served as the origin of failure in the weaker samples of all the material groups evaluated.

5.2 Future Work

1. Extensive evaluations on the effect of thermal cycling of the MMA materials should be performed as the current studies account only for the initial phase of the 1000s of cycles that these materials may undergo during actual operation.

2. FEM simulations of porous MMA tube materials with random distribution of pores and flaws should be conducted to study the stress distribution and identify probable failure modes. Furthermore, X-ray tomography can be utilized to generate meshed geometry from the actual MMA tube materials, which can be used to perform FEM simulations.

3. Microscopic and fractographic evaluations of all the materials should be conducted to correlate the grain structure, porosity, flaw size and orientation with the mechanical reliability, strength distributions and slow crack growth properties.

CHAPTER 6 : REFERENCES

[1] A. B. Stambouli and E. Traversa, “Solid oxide fuel cells (SOFCs): A review of an environmentally clean and efficient source of energy,” *Renew. Sustain. Energy Rev.,* vol. 6, no. 5, pp. 433–455, 2002.

[2] B. Tanç, H. T. Arat, E. Baltacıoğlu, and K. Aydın, “Overview of the next quarter century vision of hydrogen fuel cell electric vehicles,” *Int. J. Hydrogen Energy*, vol. 44, no. 20, pp. 10120–10128, 2019.

[3] H. Kawamoto, “Research and Development Trends in Solid Oxide Fuel Cell Materials,” *Sci. Technol. Trends*, vol. 26, no. 1, pp. 52–70, 2008.

[4] EG & G Services & National Energy Technology Laboratory, “Fuel Cell Handbook (Seventh Handbook),” Morgantown, West Virginia, 2004.

[5] V. S. Bagotsky, *Fuel Cells - Problems and Solutions*, 2nd ed. John Wiley & Sons, Inc, 2012.

[6] K. Kendall, “Introduction to SOFCs,” in *High-Temperature Solid Oxide Fuel Cells for the 21st Century*, 2nd ed., no. 2, Academic Press, 2016, pp. 1–22.

[7] R. Berke, M. E. Walter, and T. Proulx, “Mechanical Characterization and Modeling of Solid Oxide Fuel Cells and Stacks,” in *The Proceedings of Experimental and Applied Mechanics*, 2011, vol. 6, pp. 37–44.

[8] K. An, “Mechanical Properties and Electrochemical Durability of Solid Oxide Fuel Cells,” Ph. D dissertation, Virginia Polytechnic Institute and State University, 2003.

[9] F. Ramadhani, M. A. Hussain, H. Mokhlis, and S. Hajimolana, "Optimization strategies for Solid Oxide Fuel Cell (SOFC) application: A literature survey," *Renew. Sustain. Energy Rev*., vol. 76, pp. 460–484, 2017.

[10] J. Wei, "Mechanical Characterization of Solid Oxide Fuel Cells and Sealants," Ph.D. dissertation, RWTH Aachen University, 2016.

[11] F. S. da Silva and T. M. de Souza, "Novel materials for solid oxide fuel cell technologies: A literature review," *Int. J. Hydrogen Energy*, vol. 42, no. 41, pp. 26020–26036, 2017.

[12] H. L. Frandsen et al., "Accelerated creep in solid oxide fuel cell anode supports during reduction," J. Power Sources, vol. 323, pp. 78–89, 2016.

[13] M. Radovic, E. Lara-curzio, and G. Nelson, "Fracture Toughness and Slow Crack Growth Behavior of Ni-YSZ and YSZ as a Function of Porosity and Temperature," in *The Proceedings of Advances in Solid Oxide Fuel Cells*, 2007, pp. 373–382.

[14] A. J. Stark, "Evaluations on the Durability of Magnesia Magnesium Aluminate (MMA) Solid Oxide Fuel Cell Materials," M.S Thesis, University of Washington, 2017.

[15] R. Danzer, P. Supancic, J. Pascual, and T. Lube, "Fracture statistics of ceramics – Weibull statistics and deviations from Weibull statistics," *Eng. Fract. Mech*., vol. 74, no. 18, pp. 2919–2932, 2007.

[16] H. Miyasato, H. Okamoto, S. Usui, A. Miyamoto, and Y. Ueno, "The Effect of Grinding on Strength of Hot- pressed Silicon Nitride," *ISIJ Int*., vol. 29, no. 9, pp. 726–733, 1989.

[17] Y. Zou, "Thermomechanical Characterization of Advanced Ceramic Membrane Materials," Ph.D. dissertation, RWTH Aachen University, 2017.

[18] J. B. Watchman, W. Roger Cannon, and M. John Matthewson, *Mechanical Properties of Ceramics*, 2nd ed. John Wiley & Sons, Inc, 2009.

[19] R. W. Rice, J. J. Mecholsky, S. W. Freiman, and S. M. Morey, "Failure Causing Defects in Ceramics: What NDE Should Find Failure Causing Defects in Ceramics: What NDE Should Find," in *The Proceedings of Review of Progress in Quantitative NDE*, 1978, pp. 257–272.

[20] H. Kim, K. Matsumaru, and A. Takata, "Reduction of Ceramic Machining Defects by Regulated Force-Feeding Grinding System," *Adv. Technol. Mater. Mater. Process*., vol.6, no. 2, pp. 290–297, 2004.

[21] R. W. Rice, "Pores as fracture origins in ceramics," *J. Mater. Sci*., vol. 19, no. 3, pp. 895–914, 1984.

[22] R. W. Rice, "Relation of Tensile Strength-Porosity Effects in Ceramics to Porosity Dependence of Young' s Modulus and Fracture Energy, Porosity Character and Grain Size," *Mater. Sci. Eng. A*, vol. 112, no. 1, pp. 215–224, 1989.

[23] P. Auerkari, "Mechanical and physical properties of engineering alumina ceramics," Espoo, Finland, 1996.

[24] ASTM C1161, "Standard Test Method for Flexural Strength of Advanced Ceramics at Ambient Temperature," *Annu. B. ASTM Stand*., vol. 18, no. 1, pp. 1–16, 2008.

[25] Waloddi Weibull, "A Statistical Distribution Function of Wide Applicability," *J. Appl. Mech*., vol. 18, pp. 293–297, 1951.

[26] G. D. Quinn and R. Morrell, "Design Data for Engineering Ceramics: A Review of the Flexure Test," *J. Am. Ceram. Soc*., vol. 74, no. 9, pp. 2037–2066, 1991.

[27] A. Chudnovsky, “Slow crack growth, its modeling and crack-layer approach: A review,” *Int. J. Eng. Sci*., vol. 83, pp. 6–41, 2014.

[28] A. Evans, “Slow crack growth in ceramic materials at elevated temperatures,” *Metall. Trans. A, Phys. Metall. Mater*., vol. 6, no. 4, pp. 707–716, 1975.

[29] N. Van Der Laag, “Environmental effects on the fracture of oxide ceramics,” Ph.D. dissertation, Eindhoven University of Technology, 2002.

[30] S. Sinhamahapatra, H. S. Tripathi, and A. Ghosh, “Densification and properties of magnesia-rich magnesium-aluminate spinel derived from natural and synthetic raw materials,” *Ceram. Int*., vol. 42, no. 4, pp. 5148–5152, 2016.

[31] C. C. Gonzaga, P. F. Cesar, W. G. Miranda, and H. N. Yoshimura, “Slow crack growth and reliability of dental ceramics,” *Dent. Mater*., vol. 27, no. 4, pp. 394–406, 2011.

[32] R. W. Rice and C. C. Wu, “Slow crack growth in MgAl2O4 single- and poly-crystals,” *J. Mater. Sci. Lett*., vol. 14, pp. 723–727, 1995.

[33] T. Pfingsten and K. Glien, “Statistical Analysis of Slow Crack Growth Experiments,” *J.Eur.Ceram. Soc*., vol. 26, no. 15, pp. 3061–3065, 2006.

[34] U. G. Bossel, “Solid Oxide Fuel Cells for Transportation,” *J. KONES Intern. Combust. Engines*, vol. 12, no. 3, pp. 43–50, 2005.

[35] “Nissan announces development of the world’s first SOFC-powered vehicle system that runs on bio-ethanol electric power - Global Newsroom.” [Online]. Available: https://newsroom.nissan-global.com/releases/160614-01-e. [Accessed: 06-May-2019].

[36] “e-Bio Fuel-Cell | NISSAN | TECHNOLOGICAL DEVELOPMENT ACTIVITIES.” [Online].Available:https://www.nissanglobal.com/EN/TECHNOLOGY/OVERVIEW/e_bio_fuel_cell.html. [Accessed: 05-May-2019].

[37] “Nissan unveils world’s first Solid-Oxide Fuel Cell vehicle - Nissan Online Newsroom.” [Online]. Available: https://nissannews.com/en-US/nissan/usa/releases/nissan-unveilsworld-s-first-solid-oxide-fuel-cell-vehicle. [Accessed: 05-May-2019].

[38] E. Lara-Curzio, M. Radovic, R. M. Trejo, C. Cofer, T. R. Watkins, and K. L. More, “Effect of Thermal Cycling and Thermal Aging on Ni-YSUYSZ Bi-Layers,” in *The Proceedings of Advances in Solid Oxide Fuel Cells*, 2007, pp. 383–391.

[39] F. Beer, E. R. Johnston, J. T. Dewolf, and D. F. Mazurek, *Mechanics of Materials*, 6th ed. New York: McGraw Hill, 2012.

[40] W. D. Callister and D. G. Rethwisch, *Materials Science and Engineering: An Introduction*, 8th ed. John Wiley & Sons, Inc, 2010.

[41] Z. Li, B. L. Wang, K. F. Wang, and L. Zheng, “A multi-scale model for predicting the thermal shock resistance of porous ceramics with temperature-dependent material properties,” *J. Eur. Ceram. Soc*., vol. 39, pp. 2720–2730, 2019.

[42] C. Aksel, B. Rand, F. L. Riley, and P. D. Warren, “Thermal shock behaviour of magnesia-spinel composites,” *J. Eur. Ceram. Soc*., vol. 24, no. 9, pp. 2839–2845, 2004.

[43] R. Grasset-bourdel, A. Alzina, M. Huger, D. Gruber, H. Harmuth, and T. Chotard, “Influence of thermal damage occurrence at microstructural scale on the thermomechanical behaviour of magnesia – spinel refractories,” *J. Eur. Ceram. Soc*., vol. 32, no. 5, pp. 989–999, 2012.

[44] E. Yalamaç, “Effect of spinel addition on the sintering behavior and microstructure of alumina-spinel ceramics,” *Ceram. Silikaty*, vol. 58, no. 4, pp. 314–319, 2014.

[45] N. Canikoğlu and H. Ö. Toplan, “Production of Magnesia-Rich Magnesium Aluminate Spinel,” in *Proceedings of 18th International Metallurgy & Materials Congress*, 2016, pp. 188–191.

[46] R. Sarkar, A. Ghosh, and S. K. Das, “Reaction sintered magnesia rich magnesium aluminate spinel: Effect of alumina reactivity,” *Ceram. Int.*, vol. 29, no. 4, pp. 407–411, 2003.

[47] C. Aksel, P. D. Warren, and F. L. Riley, “Fracture behaviour of magnesia and magnesia spinel composites before and after thermal shock,” *J. Eur. Ceram. Soc.*, vol. 24, no. 8, pp. 2407–2416, 2004.

[48] N. Batrakov, A. Gaprindashvili, and I. Fedotov, “Refractories based on the system periclase–spinel,” *Refractories*, vol. 15, no. 11, pp. 769–771, 1974.

[49] C. B. Carter and M. G. Norton, *Ceramic Materials: Science and Engineering*, 2nd ed. Springer US, 2013.

[50] George D. Quinn and Janet B. Quinn, “Reporting Strengths of Dental Materials,” *Dent Mater*, vol. 26, no. 2, pp. 135–147, 2011.

[51] B. Bergman, “On the estimation of the Weibull modulus,” *J. Mater. Sci. Lett.*, vol. 8, no. 3, pp. 689–692, 1984.

[52] K. C. Kapoor and L. R. Lamberson, *Reliability in Engineering Design*, 1st ed. John Wiley and Sons, USA, 1977.

[53] ASTM C1368-18, “Standard Test Method for Determination of Slow Crack Growth Parameters of Advanced Ceramics by Constant Stress-Rate Strength Testing at Ambient Temperature,” *Annu. B. ASTM Stand*., vol. 15, pp. 1–11, 2001.

[54] S. Bandopadhyay and N. Nagabhushana, “Crack Growth Analysis of Solid Oxide Fuel Cell Electrolytes,” Fairbanks, Alaska, 2003.

[55] F. Fleischhauer, A. Tiefenauer, T. Graule, R. Danzer, A. Mai, and J. Kuebler, “Failure analysis of electrolyte-supported solid oxide fuel cells,” *J. Power Sources*, vol. 258, pp. 382–390, 2014.

[56] F. Fleischhauer, R. Bermejo, R. Danzer, A. Mai, T. Graule, and J. Kuebler, “High temperature mechanical properties of zirconia tapes used for electrolyte supported solid oxide fuel cells,” *J. Power Sources*, vol. 273, pp. 237–243, 2015.

[57] S. R. Choi and N. P. Bansal, “Flexure strength, fracture toughness, and slow crack growth of YSZ/alumina composites at high temperatures,” *J. Am. Ceram. Soc*., vol. 88, no. 6, pp. 1474–1480, 2005.

[58] F. Fleischhauer et al., “Fracture toughness and strength distribution at room temperature of zirconia tapes used for electrolyte supported solid oxide fuel cells,” *J. Power Sources*, vol. 275, pp. 217–226, 2015.

[59] Y. C. Zhang, H. Q. Zhao, W. Jiang, S. T. Tu, X. C. Zhang, and R. Z. Wang, “Time dependent failure probability estimation of the solid oxide fuel cell by a creep-damage related Weibull distribution model,” *Int. J. Hydrogen Energy*, vol. 43, no. 29, pp. 13532– 13542, 2018.

[60] G. Pecanac, S. Foghmoes, M. Lipinska-Chwałek, S. Baumann, T. Beck, and J. Malzbender, “Strength degradation and failure limits of dense and porous ceramic membrane materials,” *J. Eur. Ceram. Soc*., vol. 33, pp. 2689–2698, 2013.

[61] F. Greco, H. Lund, A. Nakajo, M. Find, and J. Van, “Modelling the impact of creep on the probability of failure of a solid oxide fuel cell stack,” *J. Eur. Ceram. Soc*., vol. 34, no. 11, pp. 2695–2704, 2014.

[62] V. Stournari, W. Deibert, M. E. Ivanova, C. Krautgasser, R. Bermejo, and J. Malzbender, “Mechanical Properties of Tape Casted Lanthanum Tungstate for Membrane Substrate Application Mechanical properties of tape casted Lanthanum Tungstate for membrane substrate application,” *Ceram. Int*., vol. 42, no. 14, pp. 15177–15182, 2016.

[63] S. R. Choi and N. P. Bansal, “Processing and Mechanical Properties of Various Zirconia/ Alumina Composites for Fuel Cell Applications,” Cleveland, Ohio, 2002.